Modeling Seismic Hazard and Landslide Occurrence Probabilities in Northwestern Yunnan, China: Exploring Complex Fault Systems with multi-segment rupturing in a Block Rotational Tectonic Zone

Jia Cheng[1*], Chong Xu[2], Xiwei Xu[1], Shimin Zhang[2], Pengyu Zhu[2]

1. School of Earth Sciences and Resources, China University of Geosciences (Beijing), Beijing, 100083, China

2. National Institute of Natural Hazards, Ministry of Emergency Management of China, Beijing, 100085, China

*Corresponding author:

Jia Cheng (jiacheng@cugb.edu.cn, jiacheng@gmail.com)

Address: China University of Geosciences (Beijing), No. 29, Xueyuan Road, Haidian, Beijing, 100083, China

Phone: +86-10-13466515670

Fax: +86-10-82322264

Abstract

The Northwestern Yunnan Region, located on the southeastern edge of the Tibetan Plateau, is characterized by a combination of ductile flow of the lower crust with low shear-wave velocity and gravitational collapse, giving rise to a complex network of active faults. This presents significant seismic hazards, particularly due to the potential for multi-segment ruptures and resulting landslides. This article presents a new seismic hazard model for the Northwestern Yunnan Region, incorporating recent findings on

fault geometry and slip rates along with historical seismicity rates to assess multi-segment rupturing risks. Among the four potential multi-segment rupture combination models examined, Model 1, characterized by multi-segment rupture combinations on single faults, particularly fracturing the Zhongdian fault, is proposed as the most suitable for the Northwestern Yunnan Region, given that the non-mainshock slip ratios on fault segments are all below the 30%~40% threshold, as supported by the agreement of modeled seismicity rates with fault slip rates. Our analysis demonstrates that the Peak Ground-motion Acceleration (PGA) values for a mean return period of 475 years, which is calculated with the developed probabilistic seismic hazard model, has a strong correlation with the spatial distribution of the faults. On average, these values are higher than the PGA given by the China Seismic Ground Motion Parameters Zonation Map. Furthermore, we utilized PGA values with the Bayesian Probability Method and a Machine Learning Model to predict landslide occurrence probabilities, as a function of our PGA distribution map. Our findings underscore that the observed combinations of multi-segment ruptures and their associated behaviors were in alignment with the small block rotation triggered by the gravitational collapse of the Tibetan Plateau. This result highlights the intricate interplay between multi-segment rupturing hazards and regional geological dynamics, while also providing valuable guidance for disaster preparedness efforts.

Key Words

Northwestern Yunnan Region; multi-segment rupture; probability seismic hazard analysis; landslide risk

1. Introduction

The collision of the Eurasian Platea and the Indian plate makes the Tibetan Plateau, the world's highest, with altitude of 4000+ m averagely. The eastern extrusion of the crust in the Tibetan Plateau, associated with the wedged Eastern Himalayan syntaxis, initiated a clockwise rotation of crustal deformation in the southeastern margin of the Tibetan Plateau (Figure 1) (Zhang et al., 2004; Gan et al., 2007; Wang and Shen, 2020). The Northwestern Yunnan Region (NWYR), in the west part of the southeastern margin of the Tibetan Plateau, borders the Tibetan Plateau, with the Lijiang-Xiaojiang fault serving as a boundary fault. This fault separates the Tibetan Plateau, boasting an average altitude of over 3000 meters, from the Yunnan Region, which maintains an average altitude of over 2000 meters (Yu et al., 2022; Zhang et al., 2022) (see Figure 1). Unlike the thrust faults along the plateau boundary, such as the Longmenshan fault ruptured by the 2008 M_W7.9 Wenchuan earthquake, the Holocene slip type of the Lijiang-Xiaojinhe fault is sinistral, with a strike-slip rate of ~ 3 mm/yr, from geological (Xu et al., 2003; Shen et al., 2005; Ding et al., 2018; Gao et al., 2019) and geodetic data (Gan et al., 2007; Cheng et al., 2012).

The peculiar slip behavior of the Lijiang-Xiaojinhe fault has garnered considerable attention in studies pertaining to crustal structure, fault activities, and earthquake hazards (Xu et al., 2003; Cheng et al., 2012; Zhao et al., 2013; Bao et al., 2015; Zhang et al., 2020; Huang et al., 2022; Zhang et al., 2022; Dai et al., 2023). Zhang et al. (2020) employed a shear-wave velocity model to reveal that three faults-the Longmenshan fault, the Lijiang-Xiaojinhe fault, and the Chenghai fault-outline a low-velocity belt in

69   the lower crust. This investigation uncovered the presence of low-crustal flow beneath

70   the NWYR. Similarly, Zhang et al. (2022) utilized magnetotelluric (MT) observations

71   in the southern vicinity of the Lijiang-Xiaojinhe fault, corroborating these findings and

72   highlighting the NWYR as a conduit for ductile low-crustal flow in 10 km depth.

73   Analogously, a GPS study by Cheng et al. (2012) yielded comparable results. Upon

74   removing the rigid rotation component from the regional GPS velocity field, they

75   demonstrated a clockwise rotation driven by ductile crustal flow, particularly

76   accelerated within the NWYR. They posited that this acceleration in clockwise rotation

77   might also be intensified by the tensional drag originating from the Burma Plate. The

78   intricate network of crustal deformation encompassing the NWYR introduces

79   complexity to the slip behavior of faults. Within this area, three distinct fault slip

80   behaviors are observed: the NE-trending Lijiang-Xiaojinhe fault displays left-lateral

81   strike-slip, NW-trending faults exhibit right-lateral strike-slip, and North-South

82   trending faults demonstrate normal slip (see Figure 2). The presence of faults with

83   diverse rupture behaviors contributes to the complexity of earthquake hazards.

84   Historically, these faults have been associated with significant seismic events and

85   numerous casualties. Notably, three earthquakes with $M7+$ occurred in the NWYR: the

86   Yongsheng earthquake of 1515 ($\sim M7.5$) on the Chenghai fault, the Midu earthquake of

87   1652 ($\sim M7$) on the Red River fault, and the Dali earthquake of 1925 ($\sim M7$) on the

88   Diancangshan East fault. Additionally, the 1990 Lijiang earthquake ($M_S7.0/M_W6.6$)

89   occurred on the Yulong East fault, exhibiting dominant normal slip behavior. Historical

90   and paleo-earthquake studies suggest that nearly all of these faults have the potential to

91 generate catastrophic earthquakes (e.g., Ding et al., 2018; Ren et al., 2007; Chang et al.,

92 2014), and induced numerous landslides (Institute of Geology-State Seismological

93 Bureau, and Yunnan Seismological Bureau, 1990; Huang et al. 2021). Fieldwork studies

94 and focal mechanisms of recent earthquakes underscore the complexity of fault slip

95 behaviors in this tectonic environment (Figure 2). Both historical and instrumental

96 earthquakes have affected nearly all faults in the region, emphasizing the seismic risks

97 in NWYR. For instance, the 2013 Deqin earthquake swarm, reaching a maximum

98 magnitude of M_S5.9/M_W5.7 on August 31 (Wu et al., 2015), and the 2021 Yangbi

99 earthquake swarm, reaching a maximum magnitude of M_S5.9/M_W6.1 on May 21 (Zhou

100 et al., 2022), are noteworthy seismic events (Figure 2). The 2013 M_W5.7 Deqin

101 earthquake swarm, characterized by tensional stress, occurred at the intersection of the

102 Zhongdian fault and the southern part of the Jinshajiang fault, illustrating the

103 susceptibility of the regional stress field to disturbance. Conversely, the 2021 M_W6.1

104 Yangbi earthquake swarm occurred at the connection point of the dominant dextral

105 strike-slip faults, namely the Red River fault and the Weiqi-Qiaohou fault, representing

106 a different tectonic environment compared to the 2013 M_W5.7 Deqin earthquake swarm.

107 This distinct setting suggests that either of these two faults could be at risk of seismic

108 activity during the pre-earthquake period of the upcoming earthquakes in this region.

109 The high altitude, dense vegetation, and easily weathered conditions make it

110 challenging to obtain accurate fault slip rates, often resulting in significant uncertainties.

111 However, recent studies have provided fresh insights into slip rates and fault behaviors,

112 offering the potential to enhance the precision of seismic hazard models. For instance,

Wu et al. (2019) evaluated the Holocene dextral slip rate of the Zhongdian fault to be

~1.5±0.2 mm/yr based on displacements of water-ice remains, while Chang et al. (2014)

obtained ~2.1±0.2 mm/yr based on displacements of river terraces, both utilizing

Optically Stimulated Luminescence (OSL) dating. These values notably differ from the

right-lateral slip rate of 4-6 mm/yr estimated by Shen et al. (2001) based on gully

displacements from the last glacial period, but are more aligned with the rates derived

from GPS velocity data (Cheng et al., 2012). Incorporating these updated fault slip rates

into regional seismic hazard models has the potential to greatly improve their accuracy

and ensure the reliability of the results.

Given the inherent challenges of fieldwork studies on fault activities, only a limited

number of investigations have been conducted regarding seismic hazard analysis in the

NWYR. Among these studies, Zhou et al. (2004) conducted a micro-zonation of seismic

hazards in the NWYR. They examined regional fault activities through field surveys

and estimated the potential maximum magnitude of these faults. Their approach

involved outlining polygons around the source faults to divide them into different

potential seismic sources and calculating historical seismicity rates within these

polygons. This methodology is widely employed in seismic hazard modeling in China,

particularly in the national seismic hazard map of the China Seismic Ground Motion

Parameters Zonation Map (CSGMPZM) (Gao et al., 2015). The CSGMPZM also

utilized this methodology to assess potential maximum magnitudes and compute

seismicity rates. However, their studies often did not integrate fault geometry models,

especially fault segmentation data. Consequently, the fault geometry, including rupture

length and area, may not be accurately linked to the magnitude of large earthquakes. Furthermore, it is crucial to recognize the potential occurrence of multi-segment rupturing, which has not been documented in historical records. Similarly, seismicity rates were typically derived solely from historical earthquakes and were not synchronized with fault slip rates. Relying solely on historical earthquakes for seismicity rate calculations may lead to either overestimation or underestimation of seismic hazards.

In this article, we developed a regional seismic hazard model for the NWYR, accounting for fault slip behaviors, the potential for large earthquakes including the likelihood of multi-segment ruptures. We initially developed fault segmentation models for the primary active faults in the NWYR, drawing on recent geological research on fault segmentation and geological fault slip rates. Subsequently, we employed the SHERIFS code (Chartier et al., 2017; 2019) to simulate seismicity rates across possible multi-segment combination models. We identified the multi-segment combination model that best aligns with the majority of fault slip rates, considering fault segmentation and historical seismicity rates. Ultimately, we calculated the Peak Ground Acceleration (PGA) with a 10% probability of exceedance within 50 years using the seismicity rates from the selected fault segmentation models and the logic tree model of GMPEs analyzed to be suitable for China mainland. The exploration of multi-segment rupture combinations, along with the resultant modeled seismicity rates and PGA values, offers valuable insights into the seismic hazard present in the NWYR. By leveraging the modeled PGA values and accounting for the site response of different

157 rock type, we employed a machine learning model to compute the probability

158 distribution of landslides induced by potential seismic hazards. This increasing

159 precision and reliability will be invaluable for guiding disaster preparedness initiatives,

160 land-use planning, and infrastructure resilience strategies in the area.

161
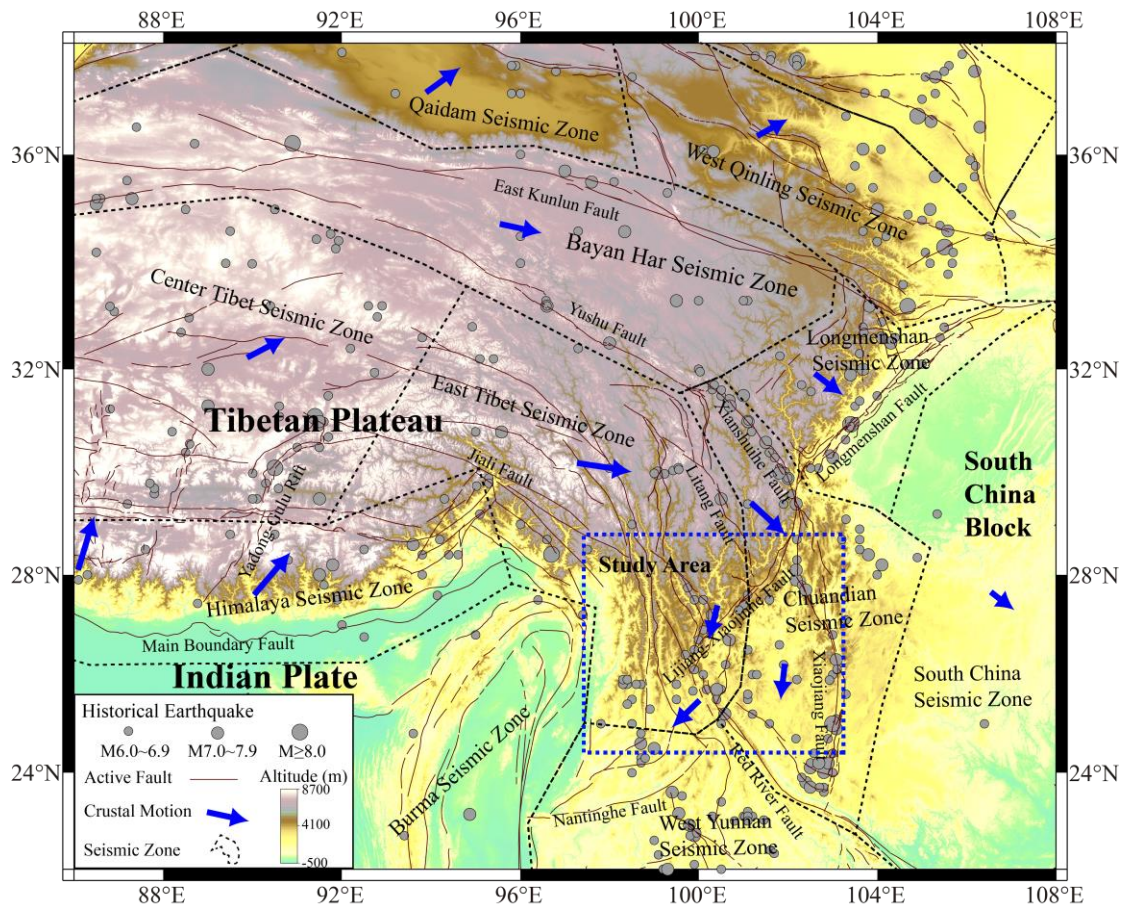
162

163 **Figure 1.** Tectonic environment of the Eastern Tibetan Plateau and the location of the

164 NWYR. The dashed rectangle delineates the study area, while dashed polygons depict

165 the seismic zones delineated by Rong et al. (2020).

166
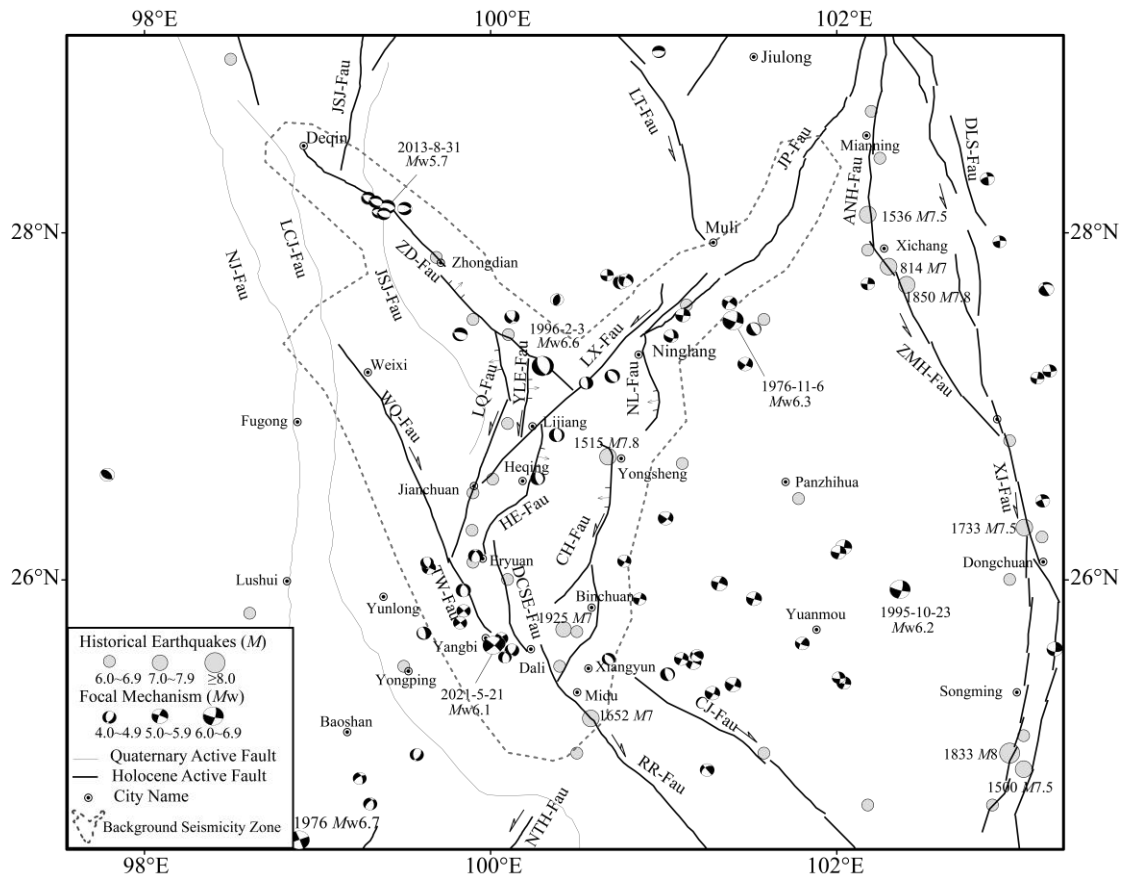
Figure 2. Regional active faults and historical earthquake activities in the NWYR. The focal mechanisms of recent earthquakes (1976~2023) are sourced from the global centroid moment tensor (GCMT) catalog. Earthquakes with $M6+$ are sourced from the moment magnitude (M_W) catalog of Cheng et al. (2017). The dashed line represents the division for background seismicity calculation, which extends 20 km from the faults. JP-Fau: Jinping fault; LT-Fau: Litang fault; ANH-Fau: Anninghe fault; ZMH-Fau: Zemuhe fault; XJ-Fau: Xiaojiang fault; CJ-Fau: Chuxiong-Jianshui fault; RR-Fau: Red River fault; NTH-Fau: Nantinghe fault; DYJ-Fau: Dayingjiang fault; NJ-Fau: Nujiang fault; LCJ-Fau: Lancangjiang fault; JSJ-Fau: Jinshajiang fault; ZD-Fau: Zhongdian fault; LX-Fau: Lijiang-Xiaojinhe fault; WQ-Fau: Weixi-Qiaohou fault; YLE-Fau: Yulong East fault; LQ-Fau: Longpan-Qiaohou fault; HE-Fau: Heqing-Eryuan fault; CH-Fau: Chenghai Fault; DCSE-Fau: Diancangshan East Fault; TW-Fau: Tongdian-Weishan Fault.

2. Fault slip rates, Segmentation, and Multi-segment Rupture Combinations

Models

2.1 Fault slip rates, Segmentation

In the NWYR, the Lijiang-Xiaojinhe fault, characterized by its left-lateral strike-slip rate, and the northern section of the Red River fault, known for its significant right-lateral strike-slip movement, play pivotal roles in crustal deformation. While the southward crustal extrusion of the Tibetan Plateau enhances the left-lateral strike-slip of the NE-trending faults like the Lijiang-Xiaojinhe fault. These observations underscore the complex interplay of fault dynamics in the NWYR, as elucidated by previous studies (Gan et al., 2007; Cheng et al., 2012; Wang and Shen, 2020). To counterbalance the southwestward crustal extrusion (Wang et al., 1998; Cheng et al., 2012), several other faults in the region, such as the Chenghai fault, the Ninglang fault, the Heqing-Eryuan fault, the Yulong East fault, and the Longpan-Qiaohou fault (also known as the Jianchuan fault), also exhibit a component of normal slip rate as well (Institute of Geology-State Seismological Bureau, and Yunnan Seismological Bureau, 1990; Han et al., 2004) (see Figure 2). In contrast, the Zhongdian fault and the northern part of the Red River fault, including the Weixi-Qiaohou fault and the Diancangshan East fault, exhibit right-lateral strike-slip movement (Zhou et al., 2004; Han et al., 2005). Recent focal mechanisms of intermediate earthquakes indicate a complex regional stress field, featuring both strike-slip and normal faulting regimes (Figure 2). Table S1 provides an overview of the observed fault slip rates in the NWYR.

The Lijiang-Xiaojinhe fault serves as a boundary fault separating the Tibetan Plateau

from the Central Yunnan block (Xu et al., 2003; Cheng et al., 2012). We divided the Lijiang-Xiaojinhe fault into 10 segments (the F1~F10 segments in Figure 3) based on fault geometry and its intersection with other faults. For the F1 segment, known as the Jinpingshan fault, recent fault mapping reveals a Holocene left-lateral slip rate ranging from 1.3 to 2.7 mm/yr derived from gully displacement across the segment, while the vertical slip rate is approximately 0.2 mm/yr (Mr. Rui Ding, 2024, private communication). Regarding the F5~F10 segments, Gao et al. (2019) demonstrated that the Hongxing-Jianshanying segment (F6 segment in Figure 3) exhibited a Holocene left-lateral slip rate of 3.32±0.22 mm/yr with a normal slip rate component of 0.35±0.02 mm/yr, whereas the Runan-Nanxi segment (F10 segment in Figure 3) had a Holocene left-lateral slip rate of 2.37±0.20 mm/yr. Accordingly, we applied the slip rate of the F6 segment to the F4~F7 segments, and the slip rate of the F10 segment to the F8~F10 segments. Notably, we considered the strike-slip motion of the F5~F10 segments to originate from two sources: the strike-slip Jinpingshan fault and the strike-slip of the Litang fault, aligning with the observed clockwise rotation of regional crustal deformation around the Litang fault and the Lijiang-Xiaojinhe fault. Consequently, we inferred the left-lateral strike-slip rate of the F4 segment to be ~2.1 mm/yr, consistent with the southern section of the Litang fault (Zhou et al., 2007). However, the F2 and F3 segments, which link the F1 and F4 segments, lack recorded fault slip rates from fieldwork studies. In this regard, we assigned a conservative estimate, employing half the value of the strike-slip rate of the F1 segment for both the F2 and F3 segments, approximately 1.2 mm/yr.

For the Longpan-Qiaohou fault (comprising the F11~F14 segments), we delineated it

into four distinct segments based on the fault mapping data provided by Wu et al. (2023).

The sinistral slip rate of the Longpan-Qiaohou fault was estimated at ~2.2 mm/yr over

the past 3500 years, with a normal slip rate of 0.23 mm/yr (Institute of Geology-State

Seismological Bureau, and Yunnan Seismological Bureau, 1990).

As for the Yulong East fault, we divided it into two segments, namely the F15 and F16

segments, utilizing fault mapping data and Quaternary sedimentary distribution. The

slip rate of the Yulong East fault was assessed by Han et al. (2005), who determined

that the Quaternary left-lateral and normal slip rates are 0.84 mm/yr and 0.70 mm/yr,

respectively, derived from the displacement observed in a gully crossing the fault.

Regarding the Zhongdian fault, we partitioned it into six segments, designated as the

F17~F22 segments, based on fault mapping data (Wu et al., 2023). The Holocene

dextral slip rate of the Zhongdian fault is estimated to be approximately 1.7-2.0 mm/yr,

with a minor normal slip rate of 0.6-0.7 mm/yr based on terrace displacement across

the fault (Chang et al., 2014).

For the Heqing-Eryuan fault, we segmented it into two sections, labeled as the F23 and

F24 segments. The Quaternary dextral slip rate and normal slip rate of the Heqing-

Eryuan fault were reported to be around 2 mm/yr and 0.7-1.0 mm/yr, respectively, as

documented by the Institute of Geology-State Seismological Bureau, and Yunnan

Seismological Bureau (1990). Additionally, recent research by Sun et al. (2017) yielded

similar fault slip rate results, indicating a left-lateral slip rate of 1.80 mm/yr and a

247   vertical slip rate of 0.28 mm/yr since the Pleistocene.

248   The Ninglang fault is primarily characterized as a left-lateral strike-slip fault, although

249   it exhibits a minor normal slip component of less than 0.1 mm/yr at the basin margin.

250   The strike-slip rate of the Ninglang fault, as determined from fault mapping work

251   conducted by Dr. Panxing Yang from Institute of Earthquake Forecasting, China

252   Earthquake Administration (2024, private communication), was estimated to be less

253   than 1 mm/yr. For our analysis, we opted to utilize a median value of 0.5±0.4 mm/yr

254   for the strike-slip rate of the Ninglang fault. Based on the distribution of Quaternary

255   sediments, we divided the Ninglang fault into two distinct segments, designated as the

256   F25 and F26 segments.

257   The sinistral slip rate of the Chenghai fault has been estimated at 2.5 to 3.0 mm/yr,

258   determined from the erosion rate of the Jinshajiang River crossing the fault.

259   Additionally, the normal slip rate is reported to be ~ 0.7-1.0 mm/yr, assessed from the

260   lift rate of the fault scarps (Institute of Geology-State Seismological Bureau, and

261   Yunnan Seismological Bureau, 1990), consistent with the findings of Tang et al. (2017).

262   We divided the Chenghai fault into three segments, i.e., the Chenghai segment (the F27

263   segment), the Qina segment (the F28 segment), and the Bingchuan segment (the F29

264   segment), based on the sedimentary distribution (Huang et al., 2018; Yu et al., 2005).

265   The southern end of the Longpan-Qiaohou fault separates the Weixi-Qiaohou fault from

266   the Tongdian-Weishan fault. We segmented these two faults into six segments each

267   based on fault mapping data and Quaternary sedimentary distribution. Concerning the

slip rate of the Tongdian-Weishan fault, the dextral slip rate in the Late Pleistocene is estimated to be ~1.8-2.4 mm/yr, with a normal slip rate of 0.17-0.35 mm/yr, calculated from the displacement of fault scarps (Chang et al., 2016).

In contrast, for the Weixi-Qiaohou fault, the dextral slip rate is ~1.25 mm/yr, while the normal slip rate is ~0.91 mm/yr since the Late Pleistocene (Ren et al., 2007). Comparing these rates to the dextral slip rate from the middle section of the Red River fault, which is reported to be 1.1 ± 0.4 mm/yr (Shi et al., 2018), it is evident that the dextral slip rates decrease from the northwest to the southeast across the Red River fault system, encompassing the Weixi-Qiaohou fault, the Tongdian-Weishan fault, and the Red River fault.

The Diancangshan East Fault is the seismogenic fault of the 1925 *M*7 Dali earthquake. We deduced that the Diancangshan East fault is a dominant normal slip fault as the boundary fault of the Dali basin and the Erhai Lake. The normal slip rate of this fault is 1-2 mm/yr (Guo et al., 1984; Zhou et al., 2004).

Additionally, we incorporated the F37 and F38 segments of the northern part of the Red River fault into our segmentation model. The right-lateral strike-slip rate of these two segments is ~1.1 mm/yr. Figure 3 illustrated the segmentation model of the faults in the NWYR.

286
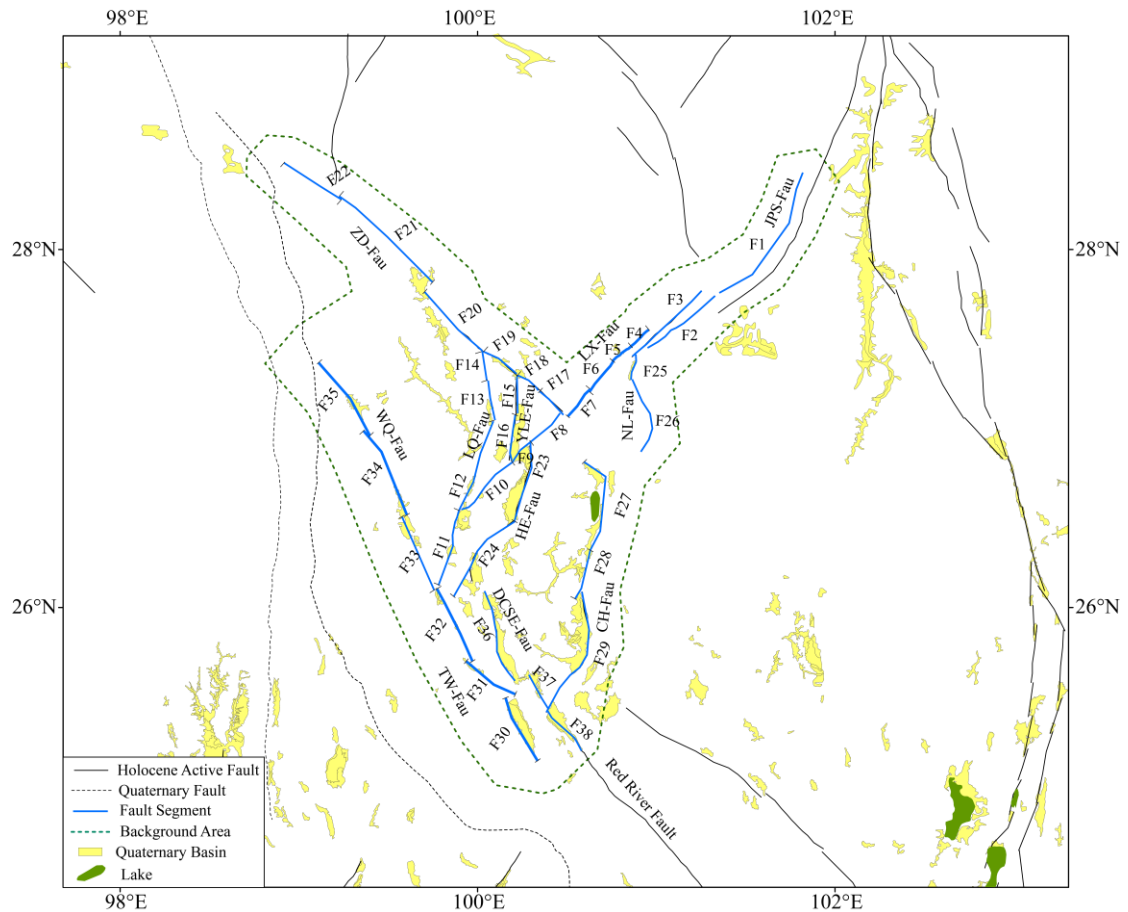
Figure 3. Fault segmentation model for the NWYR. In which, the Quaternary

Basin distribution was from Deng et al. (2003); the fault data are from Wu et al.

(2023).

2.2 Multi-segment Rupture Combinations Models

Recently, geological and geophysical studies have documented several large

earthquakes characterized by multi-segment rupturing. Notable examples include the

M_W7.4 Landers earthquake in 1992 (Campillo and Archuleta, 1993), the M_W7.9

Wenchuan earthquake in 2008 (Xu et al., 2009), the M_W7.8 Kaikoura earthquake in

2016 (Xu et al., 2018), and the 2023 doublet events of M_W7.8 and M_W7.5 in Turkey

(Petersen et al., 2023). These events exhibited rupturing across different segments,

resulting in larger magnitudes than would be expected from single-segment ruptures.

299   Numerous studies have focused on understanding the fault's geometric and

300   physical parameters to ascertain conditions conducive to multi-segment rupturing.

301   Factors identified include step width (e.g., < 5 km) (Harris and Day, 1999; Lozos et al.,

302   2012), fault structural maturity characterized by initiation age, net slip, length, and slip

303   rate (Manighetti et al., 2007; 2021), and geometric irregularities such as fault branches

304   and bends, significantly influenced by the pre-existing stress field (Mignan et al., 2015).

305   For strike-slip faults, we applied conclusions from dynamic rupture modeling,

306   indicating that a step width of more than 5 km (Harris and Day, 1999), and a strike

307   difference of more than 28°, as observed in field studies of historical rupture events

308   (Biasi and Wesnousky, 2017), could inhibit earthquake rupture, to select the multi-

309   segment rupture combinations.

310   In our segmentation model of the NWYR, the distance between the F3 segment

311   and the F1-F2 segments is approximately 7 km, and the step width between the F20 and

312   F21 segments is also about 7 km. Similarly, the distance between the F3 segment and

313   the F4 segment is approximately 6.5 km. Based on these distances, we did not consider

314   the rupture continuity of these segments. For multi-fault rupture combinations, the

315   strike difference was also used to assess whether multi-fault rupture could occur.

316   Consequently, we excluded nearly all the multi-fault rupture combinations, except for

317   the combination between the F10 and F11 segments, which have a strike difference of

318   about 20°.

319   Based on the segmentation model, fault rupture behaviors, the intersections among

320   fault segments and geometric information discussed above, we developed four multi-

321   segment rupture combination models for the fault segments in the NWYR (Figure 4).

322   The M_W6.6 Lijiang earthquake on February 3, 1996, represents a significant normal

323   rupture event that occurred on the Yulong East fault. This earthquake stands out as the

324 most substantial seismic event in the NWYR since the 1970s, underscoring the normal

325 slip behavior of the Yulong East fault. This observation suggests potential effect on the

326 multi-segment rupture behavior of the Zhongdian fault.

327   In Model 1, we exclusively examined the multi-segment rupture combinations

328 within the same faults. Specifically, for the Zhongdian fault, we included the multi-

329 segment rupturing of the F17 and F18 segments, as well as the multi-segment rupturing

330 of the F19 and F20 segments. This approach considered the normal slip behavior of the

331 Yulong East fault (F15 and F16 segments) and its potential impact on Quaternary

332 sedimentary distribution between the F18 and F19 segments of the Zhongdian fault.

333 Subsequently, in Model 2, we evaluated the plausibility of multi-segment rupturing

334 occurring across the F17~F20 segments.

335   In the NWYR, the prevailing fault behavior is sinistral slip along the northeast-

336 trending faults, a trend consistent with the observed clockwise rotation in regional

337 crustal deformation (Cheng et al., 2012) and the presence of ductile low-crust flow

338 (Zhang et al., 2022). The sinistral slip observed along the Longpan-Qiaohou fault may

339 strongly impacted on the dextral slip occurring along the Weixi-Qiaohou fault, which

340 extends from the Tongdian-Weishan fault, contributing to the decrease in dextral slip

341 rates observed from the Weixi-Qiaohou fault to the Tongdian-Weishan fault. In Model

342 3, we integrated the multi-segment rupture combination of the Weixi-Qiaohou fault (the

343 F33~F35 segments) and the Tongdian-Weishan fault (the F30~F32 segments).

344   In 2023, two earthquakes of $M_W7.8$ and $M_W7.5$ successively ruptured the East

345 Anatolia fault region in Turkey (Xu et al., 2023; Petersen et al., 2023). The rupture of

346 the first earthquake, with Mw7.8, initiated on the splay Narli fault and propagated

347 bilaterally along the main East Anatolia fault (Liu et al., 2023). Consequently, we took

348 into account the possibility of rupture propagation from one fault to another in our

349   rupture combinations. Using Model 4, we investigated whether the rupture on the

350   Lijiang-Xiaojinhe fault could propagate to the Longpan-Qiaohou fault. This

351   consideration was prompted by similarities in the rupture behavior between the F11

352   segment of the Longpan-Qiaohou fault and the F10 segment of the Lijiang-Xiaojinhe

353   fault (Table S1), along with a strike difference of ~20°, smaller than the threshold of 28°

354   proposed by Biasi and Wesnousky (2017) to prohibit the rupture process.
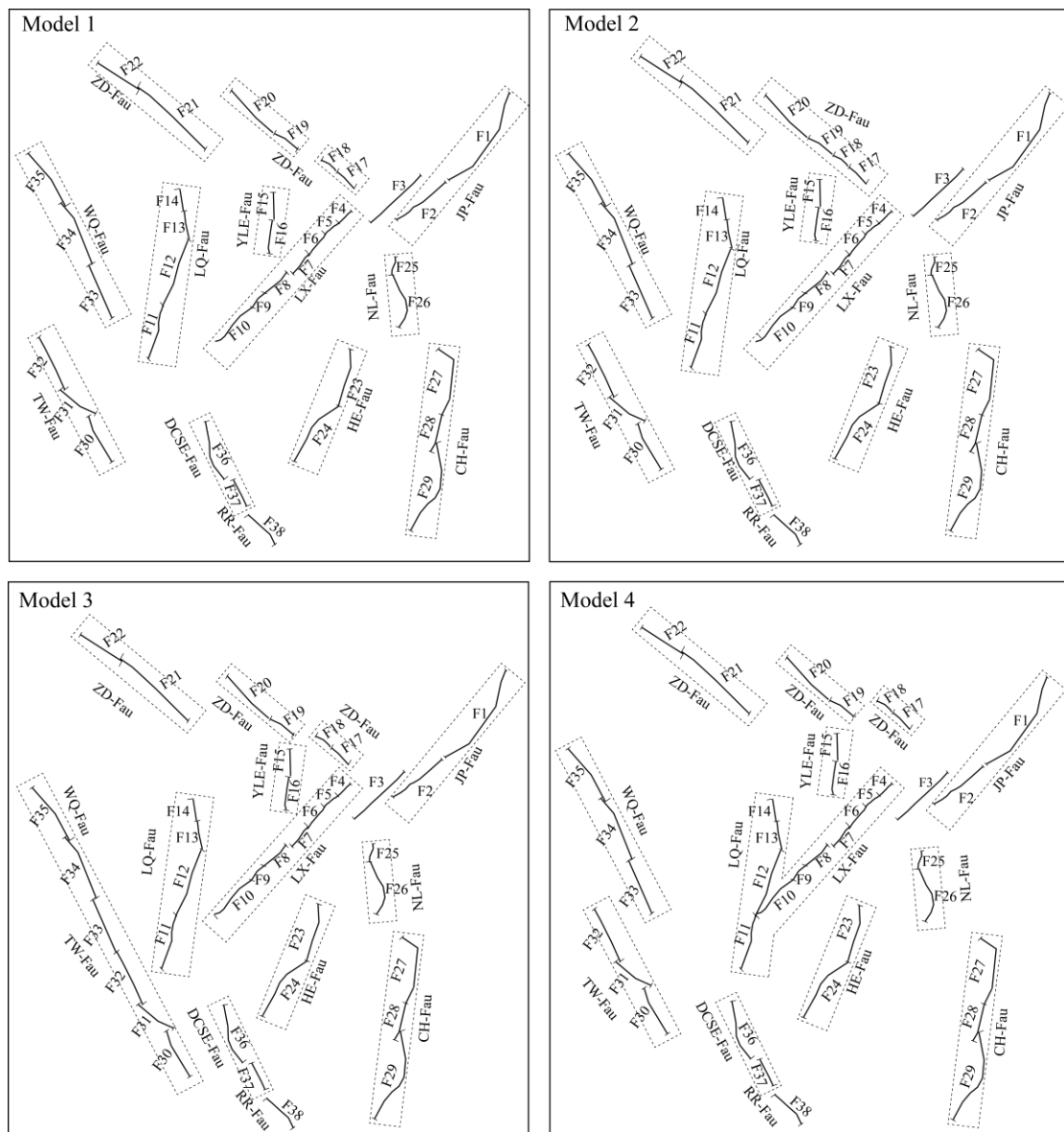
355

356   **Figure 4.** Possible Rupture Combination Models for the Fault Segments in NWYR.

357   Dashed rectangular show the rupture combinations for each Model.

358

3. Multi-segment rupture hazard Modeling

Recognizing the importance of these rupture parameters in producing multi-segment rupturing, recent studies, such as those by Chartier et al. (2019), Cheng et al. (2021), Lee et al. (2022), and Chang et al. (2023), included the possibilities and probabilities of multi-segment rupturing in seismic hazard analysis. Additionally, Dutykh et al. (2013) and Rashidi et al. (2020) employed multi-segment rupturing into models of tsunami wave generation. The concept of multi-segment rupturing was also incorporated in the UCERF3 model through their complex "Grand Inversion" methodology, which integrates data on fault slip rates, historical seismicity, and paleo-earthquake records (Page et al., 2014; Field et al., 2014). However, for most other regional studies, collecting all the necessary input parameters remains challenging.

In seismic hazard modeling, fault slip rates can be used instead of historical seismicity data to simulate seismicity rates on faults, as slip rates span multiple seismic cycles of large-magnitude earthquakes and provide estimates of the average earthquake recurrence interval (Youngs and Coppersmith, 1985). We utilize the methodology developed by Chartier et al. (2019) to translate these fault slip rates into seismicity rates, considering both multi-segment and single-segment ruptures.

3.1 Methodology

In our earthquake hazard modeling, the seismicity rates should reflect both the fault slip rate and the regional magnitude-frequency distribution (MFD), e.g., the Gutenberg-Richter (G-R) Relationship (Gutenberg and Richter, 1944) and the Characteristic earthquake model (Schwartz and Coppersmith, 1984). Youngs and Coppersmith (1995) balanced fault slip rates with MFD to determine the seismicity rate on faults. They employed the composite characteristic earthquake model (Y-C) or

truncated G-R model to convert the fault slip rate into the seismicity rates on the fault. These converted MFD were widely used in seismic hazard analysis (e.g., Avital et al., 2018; Chartier et al., 2019; Rong et al., 2020). This approach enables a more comprehensive assessment of earthquake hazards by integrating both fault slip rates and the frequency of seismic events. For assessing the possibilities and probabilities of multi-segment rupturing, it is essential to represent the seismicity rate of such combinations within the magnitude-frequency relationship for each segment.

To achieve this, Chartier et al. (2017; 2019; 2021) devised a Python-based code known as SHERIFS. This code employed an iterative process, enabling the balancing of occurrence rates for multi-segment rupturing events alongside intermediate and small earthquakes on each fault segment. Leveraging historical seismicity data, they utilized the slip rate of each fault segment to convert it into the target MFD on the fault, such as the G-R, or the Y-C distribution. This method offered a robust framework for assessing seismic hazard, integrating both single and multi-segment rupture scenarios effectively. Determining the maximum magnitudes of individual fault segments and their combinations could rely on fault length, following rupture scaling laws proposed by researchers (e.g., Wells and Coppersmith, 1994; Leonard et al., 2010; Cheng et al., 2020). Since most rupture scaling relationships are developed for plate boundary regions (Stirling et al., 2013), we selected a regression scaling relationship based on a dataset of earthquakes from China mainland (Cheng et al., 2020) and compared the results with those from the widely used rupture scaling relationship by Wells and Coppersmith (1994), which incorporates global data from both interplate and intraplate earthquakes.

In these steps, the b-value from historical earthquakes, the rupture scaling law of the faults, and the fault slip rates are typically accompanied by significant uncertainties.

408 SHERIFS used the random sampling method to explore the uncertainty bounds. The

409 rates are derived while examining uncertainties related to earthquake magnitudes, the

410 duration of the completeness period, and the limited number of observed earthquakes

411 for larger magnitudes, using a Monte Carlo approach (Chartier et al., 2021). For each

412 branch of the logic tree in the random sampling, it generates a corresponding number

413 of models that match the total count of random samples. For each model, the slip-rate

414 value is selected uniformly within its uncertainty bounds, scaling law parameters are

415 chosen independently from a Gaussian distribution within their error bounds, and the

416 b-value is picked from the user-defined range. All these uncertainties propagate to the

417 final step of calculating seismicity rates with uncertainties.

418 In the final step, they iterated the seismicity rates across magnitude bins associated

419 with multi-segment rupturing, spanning from large magnitudes down to small

420 magnitudes, according to the target MFD for each fault segment. However, in many

421 cases, the fault slip rate or the calculated seismicity rates couldn't fully account for the

422 entire seismic activity. The remaining portion of the fault slip rate for each segment was

423 attributed to non-main-shock slip (NMS), including processes like post-seismic slip and

424 silent creep. An NMS ratio of ≤30%-40% is typically considered indicative of a model

425 misfit, potentially arising from factors like creeping and specific conditions, such as

426 boundary fault segments or creeping segments. Here, we adopted a similar approach in

427 simulating seismic hazard modeling for the regional fault system in the NWYR.

428
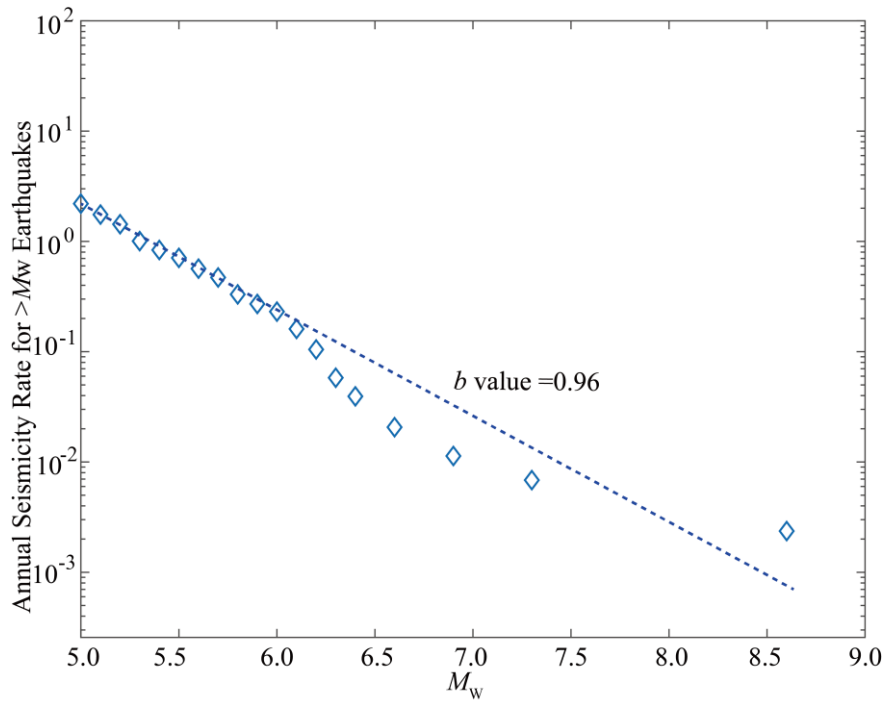
429

430 **Figure 5.** Calculated b value for the East Tibet Seismic Zone where the NWYR

431 located in Figure 1.

432

433 3.2 **Scaling Relationship and Modeling Parameters**

434   Given the fractured structure of the crust in the NWYR, as documented by Cao et

435 al. (2023), the seismicity distribution in this area was notably complex and significantly

436 different from that observed directly on the fault lines. Therefore, in our analysis of

437 seismicity rates for the regional faults, we opted to utilize the G-R relation (Gutenberg

438 and Richter, 1944) as the Magnitude-Frequency relationship, rather than the Youngs-

439 Coppersmith (Y-C) relation (Youngs and Coppersmith, 1985). For estimating

440 magnitudes based on rupture length, we applied the relationship proposed by Cheng et

441 al. (2020) to determine the maximum magnitude for each individual fault segment as

442 well as their multi-segment combinations. Additionally, we accounted for a portion of

443 earthquakes with $M<6.5$ as off-fault seismicity. Specifically, we assigned probabilities

444 of 95%, 90%, 85%, 80%, and 80% for magnitude bins of 6.0 -6.4, 5.5-5.9, 5.0-5.4, 4.5-

445 4.9, and 4.0-4.4, respectively, based on prior studies (Chartier et al., 2019; Cheng et al.,

446 2021).

447 We calculated the b-value for the East Tibet Seismic Zone, which encompasses

448 nearly all of the NWYR, as illustrated in Figure 1. The earthquake catalog utilized for

449 this analysis was sourced from Cheng et al. (2017), covering the time period from 780

450 BC to 2015 AD. Additionally, we incorporated earthquakes from the Global CMT

451 catalog spanning the period from 2016 to 2023. The regressed b-value was

452 approximately 0.96, with completeness times for magnitudes M_W4.5, M_W5.0, M_W5.3,

453 M_W5.7, M_W6.1, and M_W6.4 identified as 1985, 1966, 1928, 1916, 1916, and 1900,

454 respectively. It is noteworthy that the calculated b-value is slightly higher than the value

455 of 0.86 reported in Rong et al. (2020), likely due to the inclusion of new earthquakes

456 occurring after 2015. Figure 5 visualizes the Gutenberg-Richter relationship in the East

457 Tibet Seismic Zone, in which the b value is 0.96.

458

459 3.3 **Comparison and Selection of Modeled Results**

460 We depicted the NMS ratios and modeled seismicity rates in Figure 6. The right

461 panels showcased the NMS ratios of the segments in Model 1~4. Model 1 exhibited the

462 most balanced results between the modeled seismicity rates and historical ones. In

463 Figure 6a, all segments in Model 1 demonstrated NMS ratios smaller than 30%.

464 Chartier et al. (2019) suggested that NMS ratios below 30%-40% serve as a benchmark

465 to assess the validity of multi-segment combination models, indicating effective

466 consumption of the slip rate of each segment into seismicity rates. The left panels in

467 Figure 6b further underscored the alignment between the modeled and observed

468 seismicity rates, showing that the observed historical seismicity rates closely matches

469 the calculated rates, particularly for <M7 earthquakes.

470   Compared to Model 1, Model 2 treats segments F17~F20 as a single unit, rather

471   than separating F17~F18 and F19~F20. The left panel of Figure 6b indicates that the

472   NMS ratios for segments F11~F14 and F4~F5 exceed 40%, while the F6~F7 multi-

473   segment combination has an NMS ratio ranging from 30% to 40%, showing that the

474   combination of segments F17~F20 has an obvious impact on the seismicity rates of

475   these faults. From the right panel in Figure 6b, the historical seismicity rates for each

476   fault segment were similar to those in Model 1. However, the calculated seismicity rates

477   for each segment in Model 2 were generally lower than those in Model 1, except for a

478   slightly higher rate in the magnitude range of 6.0-6.5. This result indicated that the fault

479   slip rates are not being adequately accounted for in Model 2, unlike in Model 1 (Figure

480   6a).

481   In Model 3, the rupture combination comprised segments of F30~F35, rather than

482   considering them separately as F30~F32 and F33~F35. Most segments exhibited high

483   NMS ratios in the left panel of Figure 6c. The calculated seismicity rates were generally

484   smaller than the historical ones in the right panel of Figure 6c. Similarly, Model 4 was

485   utilized to investigate whether the great earthquakes of the Y-shaped rupture, combining

486   segments F4~F10 with F11~F14, could occur. The NMS ratio for each segment and the

487   calculated seismicity rates were comparable to those observed in Model 3 (Figure 6d).

488   In addition, we also presented the results using the rupture scaling relationship

489   proposed by Wells and Coppersmith (1994) in Figure S1. Model 1 exhibited the most

490   consistent outcomes, with the maximum NMS ratio observed on F14 at 39.3%. The

491   NMS ratios for all other segments were below 30%. For the calculated seismicity rates

492   from Model 2 to Model 4, using the rupture scaling relationship of Wells and

493   Coppersmith (1994), we observed similar patterns, with segments in all three models

494   exhibiting NMS ratios exceeding 40%. In summary, these models, utilizing the rupture

495 scaling of Wells and Coppersmith (1994), consistently yielded higher average NMS

496 ratios compared to those obtained from the rupture scaling of Cheng et al. (2020),

497 though the ratios were similar.

498
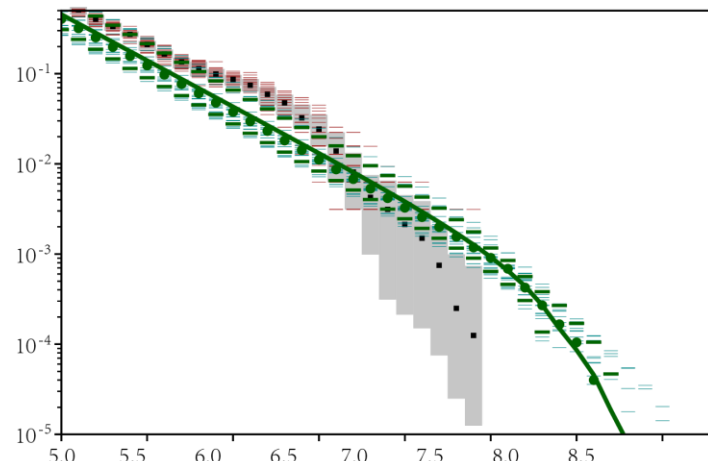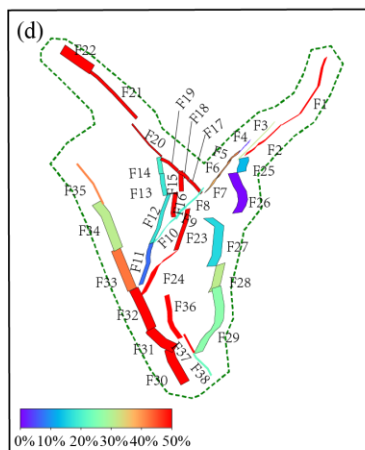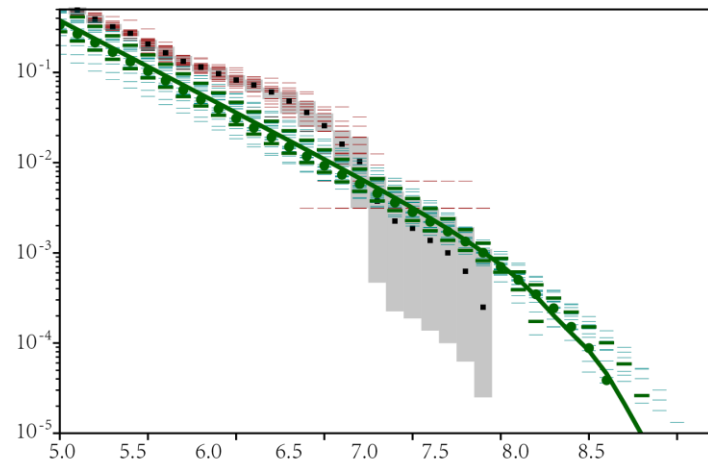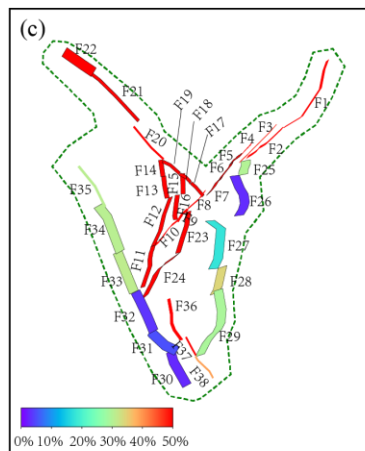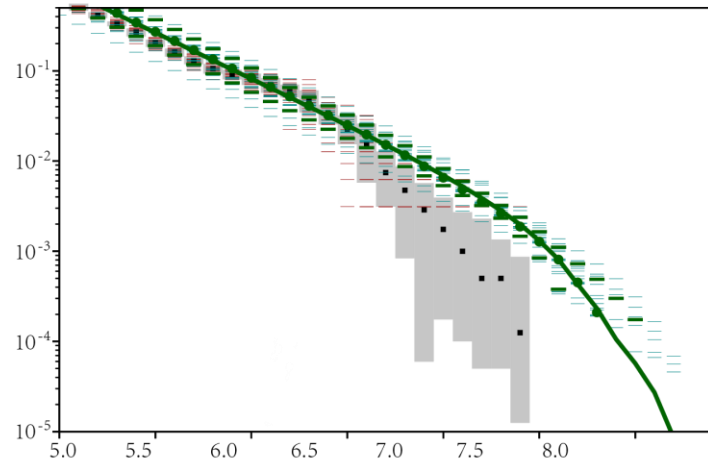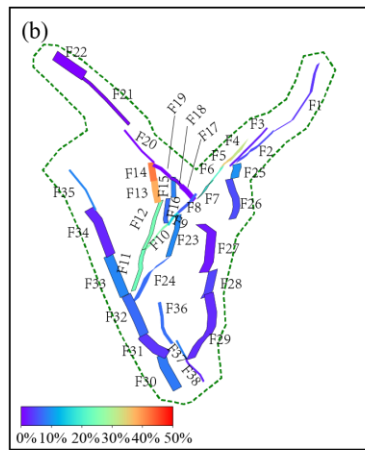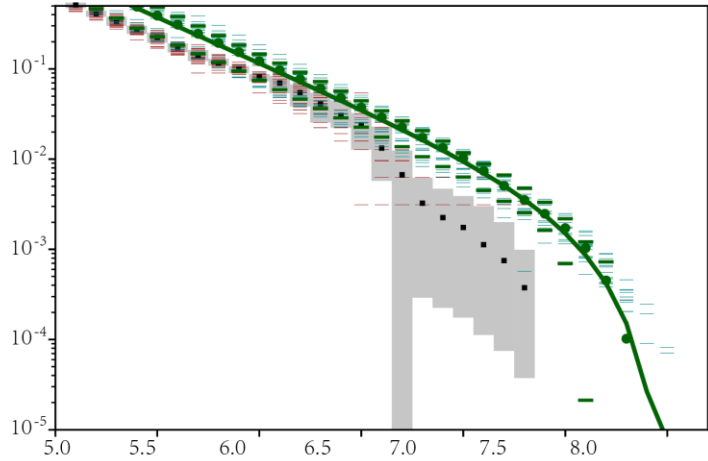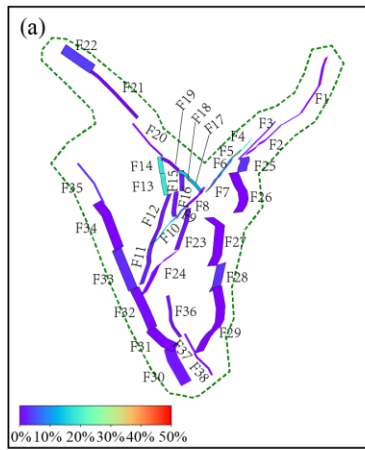
Figure 6. Calculated NMS ratios and comparison results for different models using the G-R relation and the scaling relationships from Cheng et al. (2020). **(a)** Modeled Non-Mainshock Slip (NMS) Ratio. **(b)** Comparisons between the historical Seismicity rates for different models. Dashed green lines are the MFD of each model, and the solid green line is the mean MFD, green patches represent the uncertainty (16-84 percentiles). The dotted black line is the rate from the catalog; the dashed red lines are individual Monte Carlo sampled rates of the catalog exploring the uncertainties on the magnitudes of earthquakes, and gray rectangular show the one-sigma uncertainty on the earthquake rates in statistical analysis.

Based on the comparison among different multi-segment rupture combination models, Model 1 demonstrated the most consistent results among the multi-segment rupture combinations, fault segment slip rates, and the Magnitude-Frequency relationship. Therefore, we utilized the seismicity rates from Model 1 to calculate the PGA values for the NWYR.

3.4 Comparison with National Seismic Hazard Map Results

We utilized the OpenQuake Engine v3.10 (Pagani et al., 2014) to calculate the PGA values for the NWYR. In this computation, we employed a logic tree model comprising the Abrahamson et al. (2014); Chiou and Youngs (2014); Campbell and Bozorgnia (2014); and Boore et al. (2014) branches of GMPEs, along with their associated uncertainties. Each branch was assigned an equal weight of 0.25, following the selection criteria established by Dangkua et al. (2018) for China Mainland. These Ground Motion Prediction Equations (GMPEs) are tailored for earthquakes characterized by moment magnitude (M_W) and the distance to the rupture plane (R_{rup})

523   or its surface projection (R_{JB}).

524   Figure 7a illustrates the distribution of PGA values for the site condition of firm

525   to hard rock (Vs30=760 m/s, or NEHRP B) resulting from the seismicity rates in Model

526   1, corresponding to a 10% probability of exceedance in 50 years, equivalent to a return

527   period of 475 years. The analysis revealed concentrations of high PGA values

528   exceeding 0.40 g near fault sources, particularly in areas with multiple fault sources.

529   These areas include the F2~F5 segments of the Lijiang-Xiaojinhe fault, the vicinity of

530   the Yulong East Fault (YLE-Fau), the southern part of the Zhongdian fault (ZD-Fau),

531   and the northern extent of the Heqing-Eryuan fault (HE-Fau).

532   The area around the F2~F5 segments includes three parallel faults, with the sum

533   of the strike-slip of ~3 mm/yr, makes the PGA values relatively higher. The maximum

534   magnitude for the combinations of the F17~F18 and F15~F16 segments are both

535   approximately $M_W6.6$. These areas exhibit a prevalence of moderate earthquakes with

536   short recurrence intervals and high PGA distributions over a 475-year return period.

537   The modeled seismicity rates for both the F23 and the F24 segments complied with the

538   G-R relationship, with sufficient intermediate earthquakes, contributing to the high

539   PGA values in the surrounding areas. Along the Chenghai fault, high PGA values are

540   concentrated around the F27~F28 segments with strike-slip rates of 3.0 mm/yr, but are

541   lower around the F29 segments with a strike-slip rate of 2.5 mm/yr. For the Red River

542   fault and its extensions, including the Tongdian-Weishan fault and the Weixi-Qiaohou

543   fault, high PGA values are concentrated around the F37~F38 segments and at the

544   intersection points of the F11, F32, and F32 segments.

545   Compared to the national seismic hazard map of the CSGMPZM (Gao et al., 2015)

546   (Figure 7b) for the site condition of dense soil and soft rock (Vs30 = 500 m/s, or NHERP

547   C) (Chen et al., 2021), our PGA values are consistently higher and more detailed. The

Vs30 of 500 m/s is equivalent to the Type II in the classification table of CSGMPZM, while the value of 760 m/s belongs to Type I$_1$. Table 1 presents the adjustment factors used by CSGMPZM for site amplification (Gao et al., 2015). Even when we applied these site amplification adjustment factors to convert our PGA values from type I$_1$ to type II, the PGA values would not change obviously as the adjustment are close to 1 for PGA values of 0.30-0.40 g, and 1 for PGA values of ≥0.40 g. In Figure 7b, the CSGMPZM indicates two high PGA values ranging from 0.30 to 0.40 g in the NWYR, specifically around the F23~F24 and the F27~F28 segments, respectively. In contrast, the PGA values in other areas surrounding the fault segments in our model range from 0.20 to 0.30 g.

In the development of the CSGMPZM, the region in the around China was divided into 29 large seismic source zones to calculate the parameters of the MFD. Additionally, over 1,000 potential fault sources across China were incorporated into the model. Historical seismicity rates on the MFD were employed to predict future seismic activity. This methodology led to lower anticipated seismicity rates in regions with limited historical earthquake records. The identification of potential fault sources in the CSGMPZM relied on expert opinions gleaned from research on historical surface rupture, fault segmentation, and the distribution of past earthquakes. These data sources were subsequently utilized to allocate predicted seismicity rates based on the MFD.

Furthermore, the utilization of different GMPEs in the CSGMPZM compared to our results could also contribute to variations in PGA values. The CSGMPZM utilized GMPEs from Yu et al. (2013) based on surface magnitude (M_S) and epicentral distance (Repi). Their GMPEs result in higher PGA values for distances less than 80 km but lower values for distances ≥80 km (Cheng et al., 2021). Consequently, the seismicity rates derived from fault slip rates and multi-segment rupture combinations were key

573 factors that resulted in our modeled PGA values higher than those from CSGMPZM.
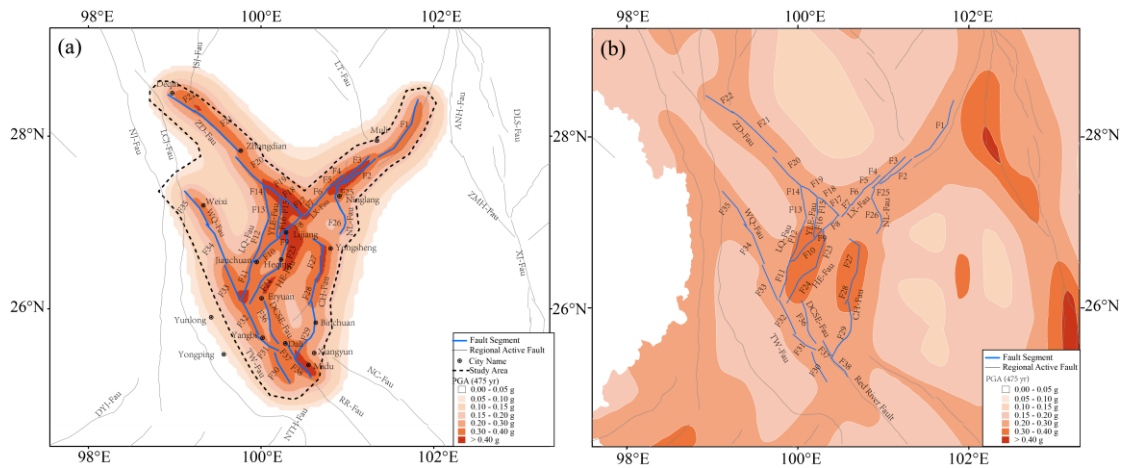
574
575 **Figure 7.** Comparison of the Modeled PGA distribution of 10% in the next 50 years.

576 **(a)** The PGA results in this article. **(b)** The PGA results in the CSGMPZM.

577
578
579 **Table 1.** Adjustment factors for PGA values of different Site condition via Type II

PGA values	Site condition type				
for type II	I_0	I_1	II	III	IV
≤0.05 g	0.72	0.80	1.00	1.30	1.25
0.10 g	0.74	0.82	1.00	1.25	1.20
0.15 g	0.75	0.83	1.00	1.15	1.10
0.20 g	0.76	0.85	1.00	1.00	1.00
0.30 g	0.85	0.95	1.00	1.00	0.95
≥0.40 g	0.90	1.00	1.00	1.00	0.90

580

581 **3.5 Validity of the Modeled Results**

582 In Figure 8, we further illustrated seismicity rates for several typical fault segments

583 to elucidate the reasons behind the observed high PGA values. Figure 8a shows the

584 seismicity rates of the F2 segment exhibit a typical G-R relationship, with a sufficient

585 number of intermediate earthquakes contributing to a high PGA distribution in the

586 surrounding area. We compared the seismicity rates on the F7~F8 segments and the F10

segment with the recurrence intervals from paleo-earthquake studies. In Figures 8b and

8c, the gray bars illustrate that our modeled seismicity rates align with the recurrence

interval of approximately 3000 years for a M_W7.5 earthquake, as reported by Ding et al.

(2018). We also observed that segments F7 to F8 of the Lijiang-Xiaojinhe fault tend to

follow the characteristic earthquake model, based on their seismicity rate distribution.

The F10 segment, approximately 44 km in length, ruptured during the 1751 M6.8

earthquake. Additionally, Tang et al. (2014) identified three paleo-earthquake events

with a recurrence interval of ~5300 years for earthquakes of M6.5+ earthquakes on the

F11 segment. They suggested that the two paleo-events prior to the 1751 AD earthquake

were considerably stronger, implying multi-segment rupturing involving combinations

of segments F11+F12, F11~F13, and F11~F14 resulting in magnitudes of M_W7.4~7.6

earthquakes. Additionally, we illustrate the seismicity rates for segments F15, F27, F29,

and F36 in Figures 8e~8f, which closely follow the G-R distribution, leading to high

PGA distributions in their vicinity. These results demonstrate that the occurrence rate

of intermediate earthquakes play a significant role in driving the high PGA distributions.
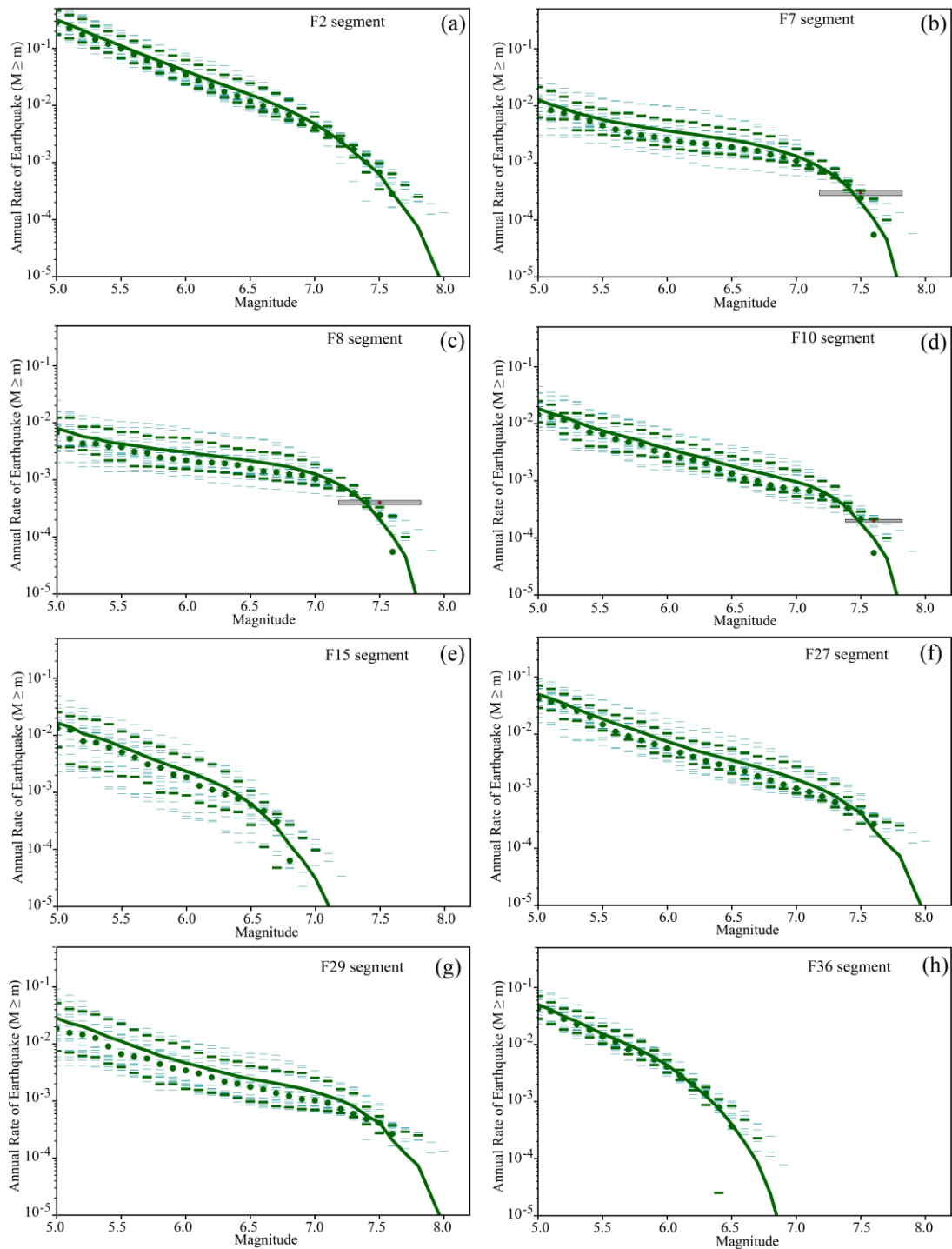
603
604 **Figure 8.** Modeled Seismicity rates for different magnitude on the fault segments. The

605 solid line is the mean MFD, and small patches represent the uncertainty (16-84

606 percentiles). The dotted line is the rate from the catalog with uncertainties. The red

607 circle is the occurrence rate of the repeated large historical earthquake rate, and the gray

608 box is the associated uncertainty.

3.6 Landslide Probabilities

3.6.1 PGA Site Amplification

Utilizing the modeled PGA values for rock site conditions presented in Figure 7a as a foundation, we enhanced our analysis by incorporating the site amplification effects derived from Chen et al.'s (2021) comprehensive site condition map. Their research, leveraging geological unit data, culminated in a detailed site condition map covering China Mainland. Leveraging this invaluable resource, we integrated their site condition map along with the amplification factors for each geological type compared to type II (referenced in Table 1) to refine the PGA value distribution map (Figure 9a). Our methodology involved multiplying the PGA values for specific site conditions by the ratio of type II PGA values to those of the specific type. This approach effectively amplified PGA values across different site conditions, enhancing the granularity of our analysis. Figure 9a illustrates the resultant PGA distribution map, now incorporates site amplifications specifically tailored for the NWYR region. Notably, our findings reveal minimal alterations in the PGA distribution, particularly near fault lines, where PGA values remain consistent or exceed 0.4 g (as detailed in Table 1).

3.6.2 Landslide Probabilities Derived from Modeled PGA Values

Using simulated ground motion data from potential earthquake scenarios, we conducted a thorough assessment of landslide susceptibility in the affected regions. Our analysis employed a machine learning framework, following the methodology outlined by Xu et al. (2019), to develop a predictive model for earthquake-induced landslides. This model was trained utilizing data from nine earthquakes, ranging from the 1999 M_W7.7 Chichi earthquake to the 2017 M_W6.5 Jiuzhaigou earthquake, all of which occurred within or near China. The training dataset comprised samples of earthquake-

induced landslides along with 13 relevant factors. These factors included various parameters such as elevation, slope angle, slope aspect, land cover, proximity to faults, geological characteristics, average annual rainfall, and PGA.

Leveraging this comprehensive dataset, we developed a robust predictive model capable of assessing landslide probabilities. We used a logistic regression model, well-regarded for its robust performance in machine learning. Unlike previous models (e.g., Nowicki et al., 2014; Wang and Rathje, 2015; Parker et al., 2017) for calculating earthquake-triggered landslide hazards, our model directly assessed the absolute probability of landslide occurrence. This probability is represented as the percentage of the landslide area within a given region relative to the total area of that region (Shao et al., 2020). As a result, our hazard estimates have a true probabilistic meaning, reflecting the actual probability of landslide occurrence rather than merely serving as a formal expression of probability. We then calculated the probabilistic seismic susceptibility for a specific point in time within the study area, producing a probabilistic PGA distribution map. By using this probabilistic PGA map as input for our model, we can estimate the corresponding probability of earthquake-triggered landslide occurrence. We employed these steps as the basis of our approach to calculating the probability of such landslides.

Figure 9b illustrates the resultant landslide probability map for the NWYR region. Notably, areas with high PGA distribution closely correspond to regions with elevated landslide probabilities. For instance, notable areas include the northern end of the Zhongdian fault, the Jinpingshan fault, the Yulong East fault, the northern end of the Heqing-Eryuan fault, the northern part of the Chenghai fault, and the eastern section of the Lijiang-Xiaojinhe fault (the F2~F4 segments). Of particular significance are regions surrounding the Yulong East fault and the convergence zone of the Lijiang-Xiaojinhe fault and the Zhongdian fault. These areas exhibit pronounced differences in elevation,

ample rainfall, and elevated PGA values, making them particularly susceptible to landslide occurrences.

By integrating multiple geospatial factors and leveraging advanced machine learning techniques, our analysis provides valuable insights into landslide susceptibility in earthquake-prone regions, aiding in effective risk management and mitigation strategies.
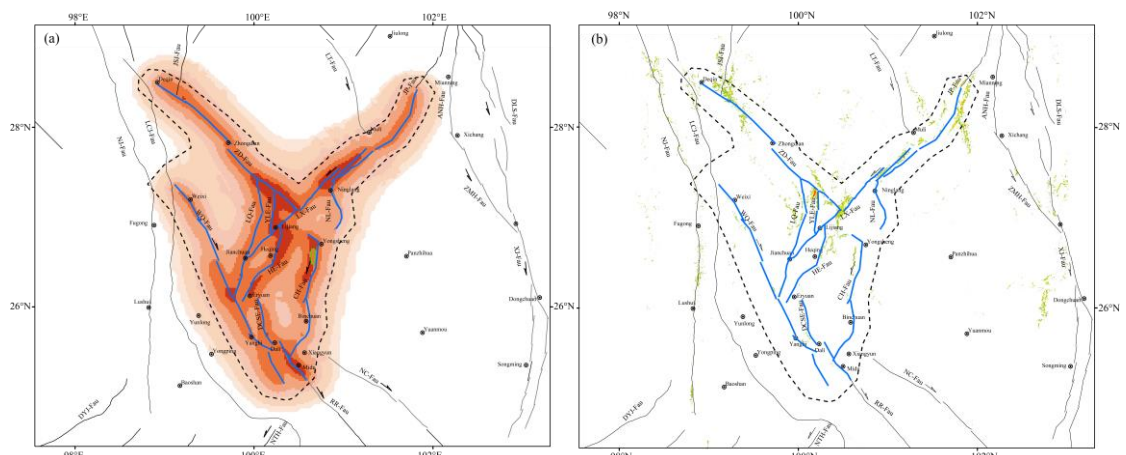
Figure 9. (a) PGA distribution Map considering different site amplifications. **(b)** Probabilities of landslide occurrence impacted by the PGA values.

4 Discussion and Conclusion

In seismic hazard analysis, understanding fault behaviors, such as slip rates and geometries, is crucial for accurately modeling future seismic activity rates. Concurrently, historical earthquake occurrence rates provide a foundational basis for estimating these future rates. Notably, attention must also be given to earthquakes involving multi-segment ruptures, which may not be fully documented in historical records. In this article, we introduce a new seismic hazard model for NWYR, where the Tibetan Plateau boundary intersects with local low-crustal flow.

4.1 Model Limitations and Mitigation Measures

Our seismic hazard modeling for NWYR represents our current understanding of average earthquake hazards in the region based on available data. The results are affected by various epistemic and aleatory uncertainties inherent in seismic hazard modeling processes, including the MFD, fault geometry, fault type, slip rate, and variability in GMPEs. Addressing the impact of these uncertainties is crucial for ensuring accurate seismic hazard assessments.

The MFD relationship, calculated from historical earthquakes, is essential for determining seismicity rate ratios across different magnitude bins. Variations in the MFD directly influences the distribution of the modeled seismicity rates. In this study, we chose the G-R relationship over the Y-C relationship due to the regional fragmented tectonic environment. The calculated b-value of 0.96 aligns closely with the expected value of 1 found in seismically active regions (Pacheco et al., 1992).

To estimate earthquake magnitudes on fault segments, we employed rupture scaling relationships based on historical rupture parameters of earthquakes in China Mainland, as proposed by Cheng et al. (2020), ensuring consistency with unique tectonic characteristics. Achieving more precise MFDs and rupture scaling laws necessitates further refinement in methodology and the use of reliable catalogs specific to the study area. Achieving more accurate MFDs and rupture scaling laws will require further methodological refinement and the use of reliable, region-specific earthquake catalogs.

For fault geometry, type, and slip rates, we relied exclusively on recent field investigation data. In compiling fault rupture models for NWYR, we analyzed these geological data under a unified tectonic stress field, ensuring coordinated fault system movements. The variability in GMPEs is complex, influenced by factors such as

701 earthquake rupture characteristics, seismic wave propagation, and site conditions.

702 Consequently, we incorporated Quaternary sediment site amplification effects on PGA

703 values. Addressing basin effects on ground motion requires dynamic simulations to

704 achieve more precise results.

4.2 Multi-segment Rupturing Hazards in NWYR

706   The complex fault system results in earthquake occurring almost all the faults with

707 various rupture behaviors in the NWYR, while the catalog of historical and paleo-

708 earthquake data only recorded a small portion of these rupturing events. The NWYR

709 serves as the boundary region between China and Myanmar. This area is predominantly

710 inhabited by ethnic minorities in China, resulting in limited written documentation of

711 its history, particularly regarding earthquake disasters.

712   Nevertheless, some significant earthquakes have been documented, particularly

713 those that impacted major cities like Dali, e.g., the 1515 M7.8 Yongsheng earthquake

714 ruptured two linked segments of the Chenghai fault (Institute of Geology-State

715 Seismological Bureau and Yunnan Seismological Bureau, 1990). The historical

716 earthquake catalog used in our seismic hazard modeling often fails to include all

717 possible rupture scenarios. To address this, we have explored reasonable models for

718 potential rupture combinations and calculate their seismicity rates.

719   These rupture combinations might be constrained by various factors, such as the

720 geometry of fault segments, the width of the step-over between each pair of segments,

721 and the maturity of the fault steps (Cunningham and Mann, 2007; Biasi and Wesnousky,

722 2017). For strike-slip faults, a step-over width of 5 km is often used to assess the

723 plausibility of the rupture combinations (e.g., Biasi and Wesnousky, 2017). However,

724 in the NWYR, where faults are situated within a conduit of ductile low-crust flow, all

step-overs are less than 5 km wide, except for the approximately 7 km step-over between the F20 and F21 segments. Hence, we advocate that the intersection relationship between faults is the primary determinant of whether multi-segment rupture events occur among fault segments in this region.

4.3 Implication of the small-block rotation in NWYR

The Holocene strike-slip motion of the Lijiang-Xiaojinhe fault plays a dominant role in this region, intersecting both the Heqing-Eryuan fault and the Yulong East fault. Model 1 also confirms the capability of the entire rupture of the F4~F10 segments of the Lijiang-Xiaojinhe fault. Additionally, the Lijiang-Xiaojinhe fault separates the Chenghai fault from the Zhongdian fault, challenging the view of Wang et al. (1998) that the Dali fault-including the Longpan-Qiaohou fault and the Chenghai fault- is the primary fault in this region. The Longpan-Qiaohou fault obstructs the westward continuation of the Lijiang-Xiaojinhe fault, and simultaneously, the F11 segment also resists rupturing in conjunction with the Lijiang-Xiaojinhe fault (Model 4 in Figure 4). In contrast, the Weixi-Qiaohou fault (WQ-F) and the Tongdian-Weishan fault (TW-F) belong to distinct small-blocks and therefore cannot rupture simultaneously, as depicted in Figure 10a. This indicates that the northern end of the Red River fault is intercepted by the Longpan-Qiaohou fault. In our model, the Zhongdian fault (ZD-F) is separated for rupture (Model 1 in Figure 4), particularly for the F17~F18 segments combination and the F19~F20 segments combination. We propose that the normal- and strike-slip of the Yulong East fault poses a greater destructive potential to the Zhongdian fault compared to the strike-slip of the Longpan-Qiaohou fault.

Hence, our multi-segment rupture configurations portrayed in Model 1 of Figure 4 align with the rotational patterns noted in the small block delineated in the NWYR by

749 Wang et al. (1998). We illustrate this clockwise rotation of the small blocks in the

750 NWYR in Figure 10a. This clockwise rotation is further supported by GPS observations

751 to the west of the Xianshuihe fault, the Anninghe fault, and the Xiaojiang fault, after

752 removal of the entire movement (Figure 10b) (Cheng et al., 2012).

753 In Figure 10b, the area where the Nujiang fault intersects with the Dayingjiang

754 fault experiences the strongest extensional forces. Rangin et al. (2013) and Lindsey et

755 al. (2023) proposed that the dynamic source of this extensional tectonic environment

756 was the side effect of the gravitational collapse of the Tibetan Plateau with the

757 westwards of upper crust faster than the lower crust (Rangin et al., 2013; Lindsey et al.,

758 2023). This extensional force significantly affects the faults in our model, driving the

759 rotation of small blocks, and the normal slip of the regional faults, e.g., the

760 Diancangshan fault and the Chenghai fault.
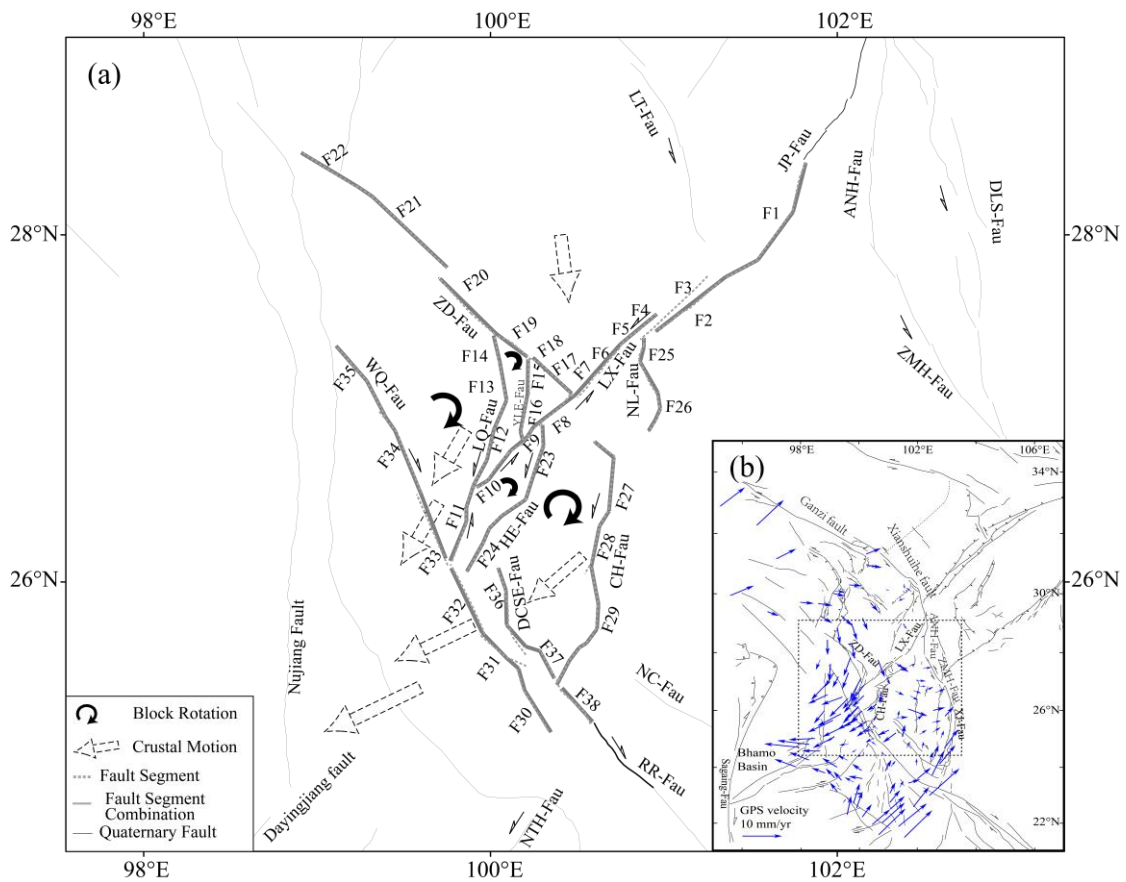
762 **Figure 10. (a)** Kinematic Model of the faults in the NWYR. **(b)** Regional GPS

motion after removing the whole movement (Cheng et al., 2012).

4.4 Conclusions

This study presents a comprehensive seismic hazard model for the NWYR, integrating fault slip rates and historical seismicity data to evaluate the risks of multi-segment ruptures and landslide occurrences. By leveraging fault slip rates and fault geometrical distributions in the NWYR, we employed the simulation method within the SHERIFS code to calculate seismicity rates for both single-segment and multi-segment ruptures. This work highlights the complexity of the fault systems within the region's block rotational tectonic environment. Our study provides valuable insights into the seismic hazards present in the NWYR. Through the development of fault segmentation models based on recent geological research and the application of advanced simulation techniques, we have significantly enhanced our understanding of fault activity and seismicity rates across the region. We also identified multi-segment models that best represent the observed data.

Our calculations of PGA with a 10% probability of exceedance within 50 years offer essential information for assessing seismic risk in the NWYR. The PGA values, associated with obvious latitude difference and abundant precipitation, increase the likelihood of landslides. Furthermore, our investigation into multi-segment rupture combinations has illuminated potential scenarios for seismic events in the region. By integration these findings, we have generated a more comprehensive assessment of seismic hazards and landslide probabilities. These factors are intertwined with the regional small block rotation induced by the low-crustal flow and gravitational collapse along the southeastern frontier of the Tibetan Plateau.

787 Future seismic hazard work can be improved by utilizing geophysical data to
788 understand fault structures where strong earthquakes are developing (Xu et al., 2017),
789 applying geodetic data to assess energy accumulation on fault segments (e.g., Yao and
790 Yang, 2023), using microseismicity relocation data to reveal fault asperities (Lay and
791 Nishenko, 2022), and employing dynamic rupture simulations of single and multi-
792 segments to enhance earthquake motion predictions (e.g., Zhang et al., 2017). These
793 studies on fault behaviors, interactions, and multi-segment ruptures are vital for
794 enhancing seismic hazard assessments. Staying vigilant and proactive in seismic risk
795 management will better protect communities and infrastructure in the NWYR and
796 beyond.

797 *Code availability*
798 In this study, we have used the code related to Chartier et al. (2019,
799 https://doi.org/10.1785/02201803320), which can be downloaded from the webpage
800 (https://doi.org/10.1785/02201803320, last accessed in May, 2024).

801

802 *Data availability*
803 The focal mechanism data are from Global CMT catalog (www.globalcmt.org, last
804 accessed in May, 2024) Table S1 in the supplementary material for this paper includes
805 the fault segments, historical and paleo-earthquakes and their associated slip parameters.

806

807 *Author contributions.*
808 Jia Cheng was responsible for methodology, software, and writing the original draft.
809 Chong Xu worked for the landslide occurrence probabilities calculation. Xiwei Xu
810 and Shimin Zhang contributed to design the fault rupture combination models.

811   Pengyu Zhu contributed to seismic hazard modeling.

812

813   *Competing interests.*

814   The authors declare that they have no known competing financial interests or personal

815   relationships that could have appeared to influence the work reported in this paper.

816

817   *Acknowledgments.*

818   We thank Dr. Guangwei Zhang from National Institute of Natural Hazards and Dr.

819   Mingming Jiang from Institue of Geology and Geophysics, Chinese Academy of

820   Sciences for discussion on the dynamic source of the crustal deformation. We are also

821   grateful to Mr. Rui Ding from National Institute of Natural Hazards and Dr. Panxing

822   Yang from Institute of Earthquake Forecasting, China Earthquake Administration for

823   their assistance in delineating fault traces and the fault segmentation work.

824   *Financial support.*

825   This study receives funds from the National Natural Science Foundation of China (No.

826   U2039201 and No. 42074064), Disciplinary Construction of Active Tectonics and

827   Earthquake hazard Chains, CUGB (No. 2023010), and National Institute of Natural

828   Hazards, Ministry of Emergency Management of China (Grant NO. ZDJ2020-14).

829

830 References

831   Abrahamson, N., Silva, W., and Kamai, R.: Summary of the ASK14 Ground Motion

832   Relation for Active Crustal Regions, Earthquake Spectra, 30, 1025-1055, 2014.

833   Avital, M., Kamai, R., Davis, M., and Dor, O.: The effect of alternative seismotectonic

834   models on PSHA results – a sensitivity study for two sites in Israel, Nature Hazards

835   and Earth System Sciences, 18, 499-514, 2018.

836   Bao, X., Sun, X., Xu, M., Eaton, D., Song, X., Wang, L., Ding, Z., Mi, N., Li, H., Yu,

D., Huang, Z., and Wang, P.: Two crustal low-velocity channels beneath SE Tibet revealed by joint inversion of Rayleigh wave dispersion and receiver functions, Earth and Planetary Science Letters, 415, 16-24, 2015.

Biasi, G., and Wesnousky, S.: Bends and ends of surface rupture, Bulletin of Seismological Society of America, 107, 2543-2560, 2017.

Boore, D., Stewart, J., Seyhan, E., and Atkinson, G.: NGA-West2 Equations for Predicting PGA, PGV, and 5% Damped PSA for Shallow Crustal Earthquakes, Earthquake Spectra, 30, 1057-1085, 2014.

Campbell, K., and Bozorgnia, Y.: NGA-West2 ground motion model for the average horizontal components of PGA, PGV, and 5% damped linear acceleration response spectra, Earthquake Spectra, 30, 1087-1115, 2014.

Campillo, M., and Archuleta, R.: A rupture model for the 28 June 1992 Landers, California, Earthquake, Geophysical Research Letters, 20, 647-650, 1993.

Cao, Y., Jin, M., Qian, J., Chen, J., and Anyiam, U.: Crustal structure and seismicity characteristics based on dense array monitoring in northwestern Yunnan, China, Physics of the Earth and Planetary Interiors, 340, https://doi.org/10.1016/j.pepi.2023.107047, 2023.

Chang, Z., Zhang, Y., Li, J., and Zang, Y.: The Geological and Geomorphic Characteristic of Late Quaternary Activity of the Deqin-Zhongdian-Daju Fault, Journal of Seismological Research, 37, 46-52, 2014 (in Chinese with English abstract).

Chang, Z., Chang, H., Zang, Y., and Dai, B.: Recent active features of Weixi-Qiaohou fault and its relationship with the Honghe fault, Journal of Geomechanics, 22, 517-530, 2016 (in Chinese with English abstract).

Chang, C., Chang, C., Gao, J., and Chan, C.: Quantifying the probability and

uncertainty of multiple-structure rupture for Taiwan, Terretrial, Atmospheric, and Oceanic Sciences, 34, https://doi.org/10.1007/s44195-023-00040-9, 2023.

Chartier, T., Scotti, O., Lyon-Caen, H., and Boiselet, A.: Methodology for earthquake rupture rate estimates of fault networks: example for the western Corinth rift, Greece, Nature Hazards and Earth System Sciences, 17, 1857-1869, 2017.

Chartier, T., Scotti, O., and Lyon-Caen, H.: SHERIFS: Open-Source code for computing earthquake rates in fault systems and constructing hazard models, Seismological Research Letters, 90, 1678-1688, 2019.

Chartier, T., Scotti, O., Lyon-Caen, H., Richard-Dinger, K., Dieterich, J. H., and Shaw, B.: Modelling earthquake rates and associated uncertainties in the Marmara Region, Turkey, Nature Hazards and Earth System Sciences, 21, 2733-2751, 2021.

Chiou, B., and Youngs, R.: Update of the Chiou and Youngs NGA Model for the Average Horizontal Component of Peak Ground Motion and Response Spectra, Earthquake Spectra, 30, 1117-1153, 2014.

Chen, G., Magistrale, H., Rong, Y., Cheng, J., Binselam, A., and Xu, X.: Seismic site condition of Mainland China from Geology, Seismological Research Letters, 92, 998-1010, 2021.

Cheng, J., Xu, X., Gan, W., Ma, W., Chen, W., and Zhang, Y.: Block model and dynamic implication from the earthquake activities and crustal motion in the southeastern margin of Tibetan plateau, Chinese Journal of Geophysics, 55, 1198-1212, 2012 (in Chinese with English abstract).

Cheng, J., Rong, Y., Magistrale, H., Chen, G., and Xu, X.: An Mw-based historical earthquake catalog for mainland China, Bulletin of Seismological Society of America, 107, 2490-2500, 2017.

Cheng, J., Rong, Y., Magistrale, H., Chen, G., and Xu, X.: Earthquake rupture scaling

relations for mainland China, Seismological Research Letters, 91, 248-261, 2020.

Cheng, J., Chartier, T., and Xu, X.: Multisegment Rupture Hazard Modeling along the Xianshuihe Fault Zone, Southeastern Tibetan Plateau, Seismological Research Letters, 92, https://doi.org/10.1785/0220200117, 2021.

Cunningham, W., and Mann, P.: Tectonics of Strike-Slip Restraining and Releasing Bends, Geological Society, London, Special Publications, 290, 1-12, 2007.

Dai, C., Gan, W., Li, Z., Liang, S., Xiao, G., Zhang, K., and Zhang, L.: Characteristics of Regional GPS Crustal Deformation before the 2021 Yunnan Yangbi Ms 6.4 Earthquake and Its Implications for Determining Potential Areas of Future Strong Earthquakes, Remote Sensing, 15, https://doi.org/10.3390/rs15123195, 2023.

Dangkua, D., Rong, Y., and Magistrale, H.: Evaluation of NGA-West2 and Chinese Ground-Motion Prediction Equations for Developing Seismic Hazard Maps of Mainland China, Bulletin of Seismological Society of America, 108, 2422-2443, 2018.

Deng, Q., Zhang, P., Ran, Y., Yang, X., Min, W., and Chu, Q.: Basic characteristics of active tectonics of China, Science China Earth Sciences, 46, 356-372, 2003.

Ding, R., Ren, J., Zhang, S., Lu, Y., and Liu, H.: Late Quaternary Paleoearthquakes on the Middle segment of the Lijiang-Xiaojinhe fault, Southeastern Tibet, Seismology and Geology, 40, 622-640, 2018 (in Chinese with English abstract).

Dutykh, D., Mitsotakis, D., Gardeil, X., and Dias, F.: On the use of the finite fault solution for tsunami generation problems, Theoretical and Computational Fluid Dynamics, 27(1-2), 177-199, 2013.

Field, E., Arrowsmith, R., Biasi, G., Bird, P., Dawson, T., Felzer, K., Jackson, D., Johnson, K., Jordan, T., Madden, C., Michael, A., Milner, K., Page, M., Parsons, T., Powers, P., Shaw, B., Thatcher, W., Weldon, R., and Zeng, Y.: Uniform

California Earthquake Rupture Forecast, version 3 (UCERF3)—The time-independent model, Bulletin of Seismological Society of America, 104(3), 1122-1180, 2014.

Gan, W., Zhang, P., Shen, Z., Niu, Z., Wang, M., Wan, Y., Zhou, D., and Cheng, J.: Present-day crustal motion within the Tibetan Plateau inferred from GPS measurements, Journal of Geophysical Research: Solid Earth, 112, https://doi.org/10.1029/2005JB004120, 2007.

Gao, M., Li, X., Xu, X., Wei, K., Yu, Y., Zhou, B., Zhao, F., Pan, H., Lv, Y., and Zhou, Q.: GB18306-2015: Introduction to the Seismic Hazard Map of China, Standards Press of China, Beijing, 1-133, 2015 (in Chinese).

Gao, Y., Ding, R., Zhang, S., and Ren, J.: Slip rate of Lijiang-Xiaojinhe fault in the Holocene, Technology for Earthquake Disaster Prevention, 14, 617-627, 2019 (in Chinese with English abstract).

Guo, S., Zhang, J., Li, X., Xiang, H., Chen, T., and Zhang, G.: Fault displacement and recurrence intervals of earthquakes at the northern segment of the Honghe fault zone, Yunnan Province, Seismology and Geology, 6, 1-12, 1984 (in Chinese with English abstract).

Gutenberg, B., and Richter, C.: Frequency of earthquakes in California, Bulletin of Seismological Society of America, 34, 185-188, 1944.

Han, Z., Guo, S., Xiang, H., Zhang, J., and Ran, Y.: Seismotectonic Environment of occurring the February 3, 1996 Lijiang M=7.0 earthquake, Yunnan Province, Acta Seismologica Sinica, 26, 410-418, 2004 (in Chinese with English abstract).

Han, Z., Xiang, H., and Guo, S.: Sinistral shear and extension of the northern section of Lijiang Basin in northwest Yunnan in Quaternary, Chinese Science Bulletin, 50, 452-459, 2005.

Harris, R., and Day, S.: Dynamic 3D simulations of earthquakes on En Echelon Faults, Geophysical Research Letters, 26, 2089-2092, 1999.

Huang, X., Wu, Z., Huang, X., and Luo, R.: Tectonic Geomorphology constrains on Quaternary Activity and Segmentation along Chenghai-Binchuan Fault zone in Northwest Yunnan, China, Earth Science, 43, 4651-4670, 2018 (in Chinese with English abstract).

Huang, X., Wu, Z., Liu, F., Tian, T., Huang, X., and Zhang, Y.: Tectonic interpretation of the main paleoseismic landslides and their distribution characteristics in the Chenghai fault zone, Northwest Yunnan, Earth Science Frontiers, 28, 125-139, 2021 (in Chinese with English abstract).

Huang, P., Gao, Y., and Xue, B.: Advances in the deep tectonics and seismic anisotropy of the Lijiang-Xiaojinhe fault zone in the Sichuan-Yunnan Block, Southwestern China, Earthquake Research Advances, 2, https://doi.org/10.1016/j.eqrea.2022.100116, 2022.

Institute of Geology-State Seismological Bureau, and Yunnan Seismological Bureau.: Active faults in Northwestern Yunnan Region, Seismological Press, Beijing, China, 1-304, 1990 (in Chinese with English abstract).

Lay, T., and Nishenko, S.: Updated concepts of seismic gaps and asperities to assess great earthquake hazard along South America, 119, https://doi.org/10.1073/pnas.2216843119, 2022.

Lee, Y., Hui, Z., Daneshvaran, S., Sedaghati, F., and Graf, W.: Impacts on catastrophe risk assessments from multi-segment and multi-fault ruptures in the UCERF3 model, Earthquake Spectra, 38, 128-151, 2022.

Leonard, M.: Earthquake Fault Scaling: Self-Consistent Relating of Rupture Length, Width, Average Displacement, and Moment Release, Bulletin of Seismological

962   Society of America, 100(5A), 1971-1988, 2010.

963 Lindsey, E., Wang, Y., Aung, L., Chong, J., Qiu, Q., Mallick, R., Feng, L., Aung, P., Tin,

964   T., Min, S., Bradley, K., Than, O., Oo, K., Thant, M., Masson, F., Bürgmann, R.,

965   and Hill, E.: Active subduction and strain partitioning in western Myanmar

966   revealed by a dense survey GNSS network, Earth and Planetary Science Letters,

967   622, https://doi.org/10.1016/j.epsl.2023.118384, 2023.

968 Liu, C., Lay, T., Wang, R., Taymaz, T., Xie, Z., Xiong, X., Irmak, T., Kahraman, M.,

969   and Erman, C.: Complex multi-fault rupture and triggering during the 2023

970   earthquake doublet in southeastern Türkiye, Nature Communication, 14,

971   https://doi.org/10.1038/s41467-023-41404-5, 2023.

972 Lozos, J., Oglesby, D., Brune, J., and Olsen, K.: Small intermediate fault segments can

973   either aid or hinder rupture propagation at stepovers, Geophysical Research Letters,

974   39, https://doi.org/10.1029/2012GL053005, 2012.

975 Manighetti, I., Campillo, M., Bouley, S., and Cotton, F.: Earthquake scaling, fault

976   segmentation, and structural maturity, Earth and Planetary Science Letters, 253,

977   429-438, 2007.

978 Manighetti, I., Mercier, A., and De Barros, L.: Fault trace corrugation and segmentation

979   as a measure of fault structural maturity, Geophysical Research Letters, 48,

980   https://doi.org/10.1029/2021GL095372, 2021.

981 Mignan, A., Danciu, L., and Giardini, D.: Reassessment of the Maximum Fault Rupture

982   Length of Strike-Slip Earthquakes and Inference on Mmax in the Anatolian

983   Peninsula, Turkey, Seismological Research Letters, 86, 890-900, 2015.

984 Nowicki, M., Wald, D., Hamburger, M., Hearne, M., and Thompson, E.: Development

985   of a globally applicable model for near real-time prediction of seismically induced

986   landslides, Engineering Geology, 173, 54-65, 2014.

987 Pacheco, J., Scholz, C., and Sykes, L.: Changes in frequency-size relationship from

988   small to large earthquakes, Nature, 355, 71-73, 1992.

989   Pagani, M., Monelli, D., Weatherill, G., Danciu, L., Crowley, H., Silva, V., Henshaw,
990   P., Butler, L., Nastasi, M., Panzeri, L., Simionato, M., and Vigano, D.: OpenQuake
991   Engine: An Open Hazard (and Risk) Software for the Global Earthquake Model,
992   Seismological Research Letters, 85, 692-702, 2014.

993   Page, M., Field, E., Milner, K., and Powers, P.: The UCERF3 Grand Inversion: Solving
994   for the Long-term rate of ruptures in a fault system, Bulletin of Seismological
995   Society of America, 104, 1181-1204, 2014.

996   Parker, R., Rosser, N., and Hales, T.: Spatial prediction of earthquake-induced landslide
997   probability, Natural Hazards and Earth System Sciences, Discussions,
998   https://doi.org/10.5194/nhess-2017-193, 2017.

999   Petersen, G. M., Büyükakpinar, P., Sanhueza, P., Metz, M., Cesca, S., Akbayram, K.,
1000   Saul, J., and Dahm, T.: The 2023 Southeast Türkiye Seismic Sequence: Rupture of
1001   a Complex Fault Network, The Seismic Record, 3, 134-143, 2023.

1002   Rangin, C., Maurin, T., and Masson, F.: Combined effects of Eurasia/Sunda oblique
1003   convergence and East-Tibetan crustal flow on the active tectonics of Burma,
1004   Journal of Asian Earth Sciences, 76, 185-194, 2013.

1005   Rashidi, A., Shomali, Z. H., Dutykh, D., and Keshavarz Farajkhah, N.: Tsunami hazard
1006   assessment in the Makran subduction zone, Natural Hazards, 100, 2, 861-875,
1007   https://doi.org/10.1007/s11069-019-03848-1, 2020.

1008   Ren, J., Zhang, S., Hou, Z., and Liu, X.: Study of Late Quaternary slip rate in the Mid-
1009   Segment of the Tongdian-Weishan fault, Seismology and Geology, 29, 756-764,
1010   2007 (in Chinese with English abstract).

1011   Rong, Y., Xu, X., Cheng, J., Chen, G., Magistrale, H., and Shen, Z.: A probabilistic
1012   seismic hazard model for mainland China, Earthquake Spectra,

1013   https://doi.org/10.1177/8755293020910754, 2020.

1014 Schwartz, D., and Coppersmith, K.: Fault behavior and characteristic earthquakes:

1015   Examples from the Wasatch and San Andreas Fault Zones, Journal of Geophysical

1016   Research, 89, 5681-5698, 1984.

1017 Shao, X., Ma, S., Xu, C., and Zhou, Q.: Effects of sampling intensity and non-slide/slide

1018   sample ratio on the occurrence probability of coseismic landslides,

1019   Geomorphology, 363, https://doi.org/10.1016/j.geomorph.2020.107222, 2020.

1020 Shen, J., Wang, Y., and Ren, J.: Quaternary dextral strike slip motion of the Deqin-Daju-

1021   Daju fault zone, Yunnan, China, in: Study on the recent deformation and dynamic

1022   of the Lithosphere of Qinghai-Xizang Plateau, edited by: Ma, Z., Wang, Y., and

1023   Zhang, Y., Seismological Press, Beijing, China, 106-122, 2001 (in Chinese with

1024   English abstract).

1025 Shen, Z., Lu, J., Wang, M., and Burgmann, R.: Contemporary crustal deformation

1026   around the southeast borderland of the Tibetan Plateau, Journal of Geophysical

1027   Research, 110, https://doi.org/10.1029/2004JB003421, 2005.

1028 Shi, X., Sieh, K., Weldon, R., Zhu, C., Han, Y., Yang, J., and Robinson, S.: Slip rate and

1029   rare large prehistoric earthquakes of the Red River fault, southwestern China,

1030   Geochemistry, Geophysics, Geosystems, 19,

1031   https://doi.org/10.1029/2017GC007420, 2018.

1032 Stirling, M., Goded, T., Berryman, K., and Litchfield, N.: Selection of Earthquake

1033   Scaling Relationships for Seismic-Hazard Analysis, Bulletin of the Seismological

1034   Society of America, 103 (6), 2993-3011, 2013.

1035 Sun, C., Li, D., Shen, X., Kang, Y., Liu, R., and Zhang, Y.: Holocene activity evidence

1036   on the southeast boundary fault of Heqing basin, middle segment of Heqing-

1037   Eryuan fault zone, West Yunnan Province. China, Journal of Mountain Science,

1038   14, 1445-1453, 2017.

1039   Tang, Y., Hu, C., Tian, Q., Wang, L., Yang, P., and Xiong, R.: A Preliminary Study of

1040   Paleo-earthquakes in the Jianchuan Section of Longpan-Qiaohou Fault Zone,

1041   Yunnan Province, Earthquake, 34, 117-124, 2014 (in Chinese with English

1042   abstract).

1043   Tang, F., Ma, H., and Song, J.: Study on the Late Quaternary activity of Chenghai fault

1044   zone, Proceeding of the 16th World conference on earthquake engineering,

1045   Santiago, Chile, 1-9, 2017.

1046   Wang, E., Burchfiel, C., Royden, L., Chen, L., Chen, L., Li, W., and Chen, Z.: Late

1047   Cenozoic Xianshuihe-Xiaojiang, Red River, and Dali Fault Systems of

1048   Southwestern Sichuan and Central Yunnan, China, Geological Society of America

1049   Special Paper, 327, 1-108, 1998.

1050   Wang, Y., and Rathje, E.: Probabilistic seismic landslide hazard maps including episte

1051   mic uncertainty, Engineering Geology, 196, 313-324, 2015.

1052   Wang, M., and Shen, Z.: Present‐Day Crustal Deformation of Continental China

1053   Derived from GPS and Its Tectonic Implications, Journal of Geophysical Research:

1054   Solid Earth, 125, https://doi.org/10.1029/2019JB018774, 2020.

1055   Wells, D., and Coppersmith, K.: New empirical relationships among magnitude, rupture

1056   length, rupture width, rupture area, and surface displacement, Bulletin of

1057   Seismological Society of America, 84, 974-1002, 1994.

1058   Wu, W., Long, F., Yang, J., Liang, M., Su, J., Wei, Y., Wu, P., and Lu, T.: Relocation,

1059   focal mechanisms and seismogenic structure of the 2013 Shangrila-Dêrong

1060   earthquake swarm sequence in the Yunnan-Sichuan border region, Chinese Journal

1061   of Geophysics, 58, 1584-1596, 2015 (in Chinese with English abstract).

1062   Wu, F., Jiang, L., Zhang, G., and Song, Z.: The fault activity and seismic hazard

assessment of central north segmentof the Deqin-Zhongdian fault, southeastern Qinghai-Tibet plateau, Acta Geologica Sinica, 93, 2657-2665, 2019 (in Chinese with English abstract).

Wu, X., Xu, X., Yu, G., Ren, J., Yang, X., Chen, G., Xu, C., Du, K., Huang, X., Yang, H., Li, K., and Hao, H.: China Active Faults Database and its web system, Earth System Science Data, https://doi.org/10.5194/essd-2023-119, 2023.

Xu, X., Wen, X., Zheng, R., Ma, W., Song, F., and Yu, G.: Pattern of latest tectonic motion and its dynamics for active blocks in Sichuan–Yunnan region, China, Science China Earth Sciences, 46, 210-226, 2003.

Xu, X., Wen, X., Yu, G., Chen, G., Klinger, Y., Hubbard, Y., and Shaw, J.: Coseismic reverse- and oblique-slip surface faulting generated by the 2008 Mw7.9 Wenchuan earthquake, China, Geology, 37, 515-518, 2009.

Xu, X., Wu, X., Yu, G., Tan, X., and Li, K.: Seismo-geological signatures for identifying $M \geqslant 7.0$ earthquake risk areas and their premilimary application in mainland China, Seismology and Geology, 39, 219-275, 2017 (in Chinese with English abstract).

Xu, W., Feng, G., Meng, L., Zhang, A., Ampuero, J., and Burgmann, R.: Transpressional rupture cascade of the 2016 Mw 7.8 Kaikoura earthquake, New Zealand, Journal of Geophysical Research: Solid Earth, 123, 2396-2409, 2018.

Xu, C., Xu, X., Zhou, B., and Shen, L.: Probability of coseismic landslides: A new generation of earthquake-triggered landslide hazard model, Journal of Engineering Geology, 27, 1122-1130, 2019 (in Chinese with English abstract).

Xu, L., Mohanna, S., Meng, L., Ji, C., Ampuero, J., Zhang, Y., Hasnain, M., Chu, R., and Liang, C.: The overall-subshear and multi-segment rupture of the 2023 Mw7.8 Kahramanmaras, Turkey earthquake in millennia supercycle, Communications Earth and Environment, 4, https://doi.org/10.1038/s43247-023-01030-x, 2023.

Yao, S., and Yang, H.: Towards ground motion prediction for potential large earthquakes from interseismic locking models, Earth and Planetary Science Letters, 601, https://doi.org/10.1016/j.epsl.2022.117905, 2023.

Youngs, R., and Coppersmith, K.: Implications of fault slip rates and earthquake recurrence models to Probabilistic Seismic Hazard estimates, Bulletin of Seismological Society of America, 75, 939-964, 1985.

Yu, W., Zhang, J., Zhou, G., Wang, J., and Zeng, X.: Surface Rupture of the 2001 Yongsheng M6 Earthquake and Chenghai Fault, Journal of Seismological Research, 28, 125-128, 2005 (in Chinese with English abstract).

Yu, Y., Li, S., and Xiao, L.: Development of ground motion attenuation relations for the new seismic hazard map of China, Technology for Earthquake Disaster Prevention, 8, 24-33, 2013 (in Chinese with English abstract).

Yu, L., Dong, Y., Zhou, W., Zhang, D., Wang, D., Yu, H., Ren, Y., and Li, J.: Evaluation of the rock uplift pattern in the Central Yunnan Subblock, SE Tibetan Plateau: Based on the Bedrock Channel Profile, Frontier in Earth Sciences, 10, https://doi.org/10.3389/feart.2022.821367, 2022.

Zhang, P., Shen, Z., Wang, M., Gan, W., Burgmann, R., Molnar, P., Wang, Q., Niu, Z., Sun, J., Wu, J., Sun, H., and You, X.: Continuous deformation of the Tibetan Plateau from global positioning system data, Geology, 32, 809-812, 2004.

Zhang, Z., Zhang, W., Chen, X., Li, P., and Fu, C.: Rupture dynamics and ground motion from potential earthquakes around Taiyuan, China, Bulletin of Seismological Society of America, 107: 1201-1212, 2017.

Zhang, Z., Yao, H., and Yang, Y.: Shear wave velocity structure of the crust and upper mantle in Southeastern Tibet and its geodynamic implications, Science China Earth Sciences, 63, 1278-1293, 2020.

1113   Zhang, J., Chen, X., Cai, J., Liu, Z., Dong, Z., Guo, C., Han, B., Jiang, F., and Cui, T.:

1114   Magnetotelluric evidence for the crustal deformation beneath the region around

1115   the Lijiang-Xiaojinhe fault, SE margin of the Tibetan Plateau, Journal of Asian

1116   Earth Sciences, 235, https://doi.org/10.1016/j.jseaes.2022.105308, 2022.

1117   Zhao, L., Xie, X., He, J., Tian, X., and Yao, Z.: Crustal flow pattern beneath the Tibetan

1118   Plateau constrained by regional Lg-wave Q tomography, Earth and Planetary

1119   Science Letters, 383, 113-122, 2013.

1120   Zhou, Q., Guo, S., and Xiang, H.: Principle and method of delineation of potential

1121   seismic sources in northeastern Yunnan Province, Seismology and Geology, 26,

1122   761-771, 2004 (in Chinese with English abstract).

1123   Zhou, R., Ye, Y., Li, Y., Li, X., He, Y., and Ge, T.: Late Quaternary activity of the

1124   Shawan segment of the Litang faults, Quaternary Sciences, 27, 45-53, 2007 (in

1125   Chinese with English abstract).

1126   Zhou, Y., Ren, C., Ghosh, A., Meng, H., Fang, L., Yue, H., Zhou, S., and Su, Y.:

1127   Seismological Characterization of the 2021 Yangbi Foreshock-Mainshock

1128   Sequence, Yunnan, China: More than a Triggered Cascade, Journal of Geophysical

1129   Research, 127, https://doi.org/10.1029/2022JB024534, 2022.